Modeling and Control of Second Life Batteries for Charging Station Applications

Master's Thesis in Sustainable Electric Power Engineering and Electromobility

Yueyan Zhang

Department of Electrical Engineering

CHALMERS UNIVERSITY OF TECHNOLOGY
Gothenburg, Sweden 2024
www.chalmers.se

Master Thesis 2024

Modeling and Control of Second Life Batteries for Charging Station Applications

Yueyan Zhang

CHALMERS
UNIVERSITY OF TECHNOLOGY

Department of Electrical Engineering
Chalmers University of Technology
Gothenburg, Sweden 2024

Modeling and Control of Second Life Batteries for Charging Station Applications
Yueyan Zhang

Supervisor: Qian Xun, RISE Research Institutes of Sweden
Examiner: Yujing Liu, Chalmers University of Technology

Master Thesis 2024
Department of Electrical Engineering
Chalmers University of Technology
SE-412 96 Gothenburg
Sweden
Telephone +46 31 772 1000

Gothenburg, Sweden 2024

Modeling and Control of Second Life Batteries for Charging Station Applications
Yueyan Zhang
Department of Electrical Engineering
Chalmers University of Technology

Abstract

Second Life Batteries (SLBs), retired from Electric Vehicles (EVs), present a promising solution for energy storage in the charging stations. Given the rapid growth of electric vehicle adoption, managing the energy demand at charging stations has become increasingly important. Utilizing SLBs can enhance sustainability and cost-efficiency by extending the lifecycle of battery systems, reducing waste and optimizing the overall energy management of charging stations. However, the integration and performance of these batteries in such applications remain underexplored, making it a critical area for research.

In this study, a comprehensive approach is taken to model and control of SLB system for use in charging stations. Firstly, a detailed modelling framework is developed to accurately represent the behavior of batteries which includes parameter identification to reflect the degradation characteristics. To facilitate the integration of these batteries into charging stations, a DC/DC converter model is incorporated. This converter topology is essential for efficiently managing the voltage levels between the SLBs and the charging stations, ensuring compatibility of the system. Additionally, the control strategy is designed to effectively manage the charging and discharging cycles of these battery modules in a charging station scenario. This also includes optimizing the voltage performance ensuring both energy efficiency and battery longevity.

The findings of this thesis highlight several key outcomes. From the modelling efforts, it is observed that SLBs exhibit specific changes in internal impedance, which must be taken into account for the reliable performance in charging stations. For the DC/DC converter, it plays a crucial role in performing proper voltage regulation between the batteries and charging stations and ensuring the system stability. In terms of control strategies, the designed approach succeeds in voltage scaling up, maintaining system stability and optimizing the operational life of the SLBs. These conclusions suggest that with appropriate modelling and control, SLBs can be an effective energy storage solution in charging stations, contributing to the broader goals of sustainability and foundations for the future integration work in charging stations.

Keywords: Battery Model, Parameter Identification, DC/DC Converter, System Stability, Battery Longevity.

Acknowledgements

Time flies, and my two years of study are coming to a fulfilling end. Throughout this academic journey, I have received tremendous care and support from many teachers, classmates, friends, and family members. I would like to express my sincere gratitude to all of them.

I would like to express my deepest gratitude to my supervisor, Dr. Qian Xun, and my examiner, Professor Yujing Liu. My supervisor provided invaluable guidance and support throughout the process of selecting a research topic, conducting the study, and writing this thesis. With great patience, Dr. Qian Xun answered my questions at every stage and helped me continuously refine my research ideas and methods. Their academic spirit and rigorous attitude have deeply influenced me, and I am incredibly grateful for their mentorship. I would also like to thank Professor Yujing Liu, whose insightful feedback as my examiner was instrumental in shaping the final version of this thesis.

Furthermore, I would like to thank my family, especially my parents. Throughout my entire academic journey, their unconditional support and encouragement have been my driving force. No matter what difficulties I encountered, they always stood behind me, providing the greatest support and giving me strength.

Lastly, I wish to thank all the friends and relatives who have helped me in my academic research and life. Your care and support have given me the confidence to reach this point and will continue to inspire me as I move forward in the future.It is because of your support and assistance that I have been able to complete this thesis. Although it may still have shortcomings, it embodies my efforts and dedication, as well as the love and expectations you have all given me. Once again, I express my most sincere thanks to all the teachers, classmates, friends, and family members who have helped me.

Yueyan Zhang, Gothenburg, July 2024

List of Acronyms

Below is the list of acronyms that have been used throughout this thesis listed in alphabetical order:

EV	Electric Vehicle
SLB	Second Life Battery
SoH	State of Health
RES	Renewable Energy System
BES	Battery Energy Storage
ICE	Internal Combustion Engine
DG	Distribution Grid
OCV	Open Circuit Voltage
SoC	State of Charge
SoH	State of Health
SEI	Solid Electrolyte Interphase
ECM	Equivalent Circuit Model
IGBT	Insulated Gate Bipolar Transistor
AC	Alternating Current
DC	Direct Current
MVAC	Medium Voltage Alternating Current
LFT	Line Frequency Transformer
MPC	Model Predictive Control
PI	Proportional-Integral

Nomenclature

Below is the nomenclature of indices, sets, parameters, and variables that have been used throughout this thesis.

Indices

t	Index for time step

Parameters

$C_{nominal}$	Nominal capacity
V_{in}	Input voltage from battery terminal
T_{on}	Conducting time for charging period in DC/DC converter
V_{out}	Output voltage from load terminal
T_{off}	Conducting time for discharging period in DC/DC converter
D	Duty cycle for DC/DC converter
L	Inductance for the DC/DC converter
F_{sw}	Switching frequency
I_{in}	Input current from battery terminal in DC/DC converter
I_{out}	Output current from load terminal in DC/DC converter
I_{peak}	Peak current over the inductor
I_{ripple}	Ripple current over the inductor
C	Capacitance of the bus capacitor in DC/DC converter
C_{rate}	Rated capacity of the battery
R_0	Resistance in battery equivalent circuit
R_1	Resistance in battery equivalent circuit
R_2	Resistance in battery equivalent circuit
C_1	Capacitance in battery equivalent circuit

C_2	Capacitance in battery equivalent circuit
i	Current flowing through R_0
i_1	Current flowing through R_1
i_2	Current flowing through C_1
i_3	Current flowing through R_2
i_4	Current flowing through C_2
V_{est}	Estimated voltage in battery parameter identification
R_{0lb}	Lower limit for component R_0 in battery equivalent circuit
R_{1lb}	Lower limit for component R_1 in battery equivalent circuit
R_{2lb}	Lower limit for component R_2 in battery equivalent circuit
C_{1lb}	Lower limit for component C_1 in battery equivalent circuit
C_{2lb}	Lower limit for component C_2 in battery equivalent circuit
R_{0ub}	Upper limit for component R_0 in battery equivalent circuit
R_{1ub}	Upper limit for component R_1 in battery equivalent circuit
R_{2ub}	Upper limit for component R_2 in battery equivalent circuit
C_{1ub}	Upper limit for component C_1 in battery equivalent circuit
C_{2ub}	Upper limit for component C_2 in battery equivalent circuit
V_{ripple}	Ripple voltage over capacitor in DC/DC converter
V_s	Input voltage of designed converter
i_L	Inductor current in DC/DC converter
Δi_L	Discretization step of inductor current
$C_{current}$	Current capacity of the battery
k_{cp}	Proportional value for the current control loop
k_{ci}	Integral value for the current control loop
k_{vp}	Proportional value for the voltage control loop
k_{vi}	Integral value for the voltage control loop

Variables

v_{out}	Output voltage from load terminal in small signal model
$\tilde{v}_{out}$	AC component of the v_{out}
d	Duty cycle in small signal model
$\tilde{d}$	AC component of the d
i_L	Indutor current in converter

$\tilde{i}_L$	AC component of the i_L
$V_{OCV(SOC)}$	Open circuit voltage at different state of charge in the battery equivalent circuit
L_{min}	Minimum value for inductor in DC/DC converter
C_{min}	Minimum value for bus capacitor in DC/DC converter

Contents

List of Figures

List of Tables

1

Introduction

1.1 Background

Greenhouse gases, including carbon dioxide (CO_2), methane (CH_4), and nitrous oxide (N_2O), play a crucial role in global warming and climate change. These gases contribute to the greenhouse effect by trapping heat within the Earth's atmosphere, leading to a rise in global temperatures. The anthropogenic increase in the concentration of greenhouse gases, primarily due to activities such as the combustion of fossil fuels, deforestation, and industrial processes, has intensified this effect, resulting in significant environmental and public health consequences. Elevated global temperatures have been linked to the increased frequency and severity of extreme weather events, such as hurricanes, heatwaves, and droughts, which in turn disrupt ecosystems, agriculture, and water resources. Moreover, the acidification of oceans, driven by higher CO_2 levels, poses a serious threat to marine life and biodiversity. Mitigating the adverse effects of greenhouse gases is imperative to address climate change and ensure a sustainable future. Figure 1.1 illustrates the continuous rise in CO_2 emissions before the pandemic, peaking at approximately 35 billion metric tons.

To mitigate the impacts of climate change, the development of electric vehicles (EVs) represents one of the most effective strategies for reducing CO_2 emissions. Electrification and automation have become increasingly integral to modern life [24]. Traditional vehicles, which rely heavily on fossil fuels, contribute significantly to environmental degradation through CO_2 emissions. Growing concerns about climate change and energy security have accelerated the adoption of renewable energy sources (RESs) over conventional energy forms. This shift is a key factor driving the rising demand for EVs. Figure 1.2 illustrates the global sales of EVs from 2014 to 2023.

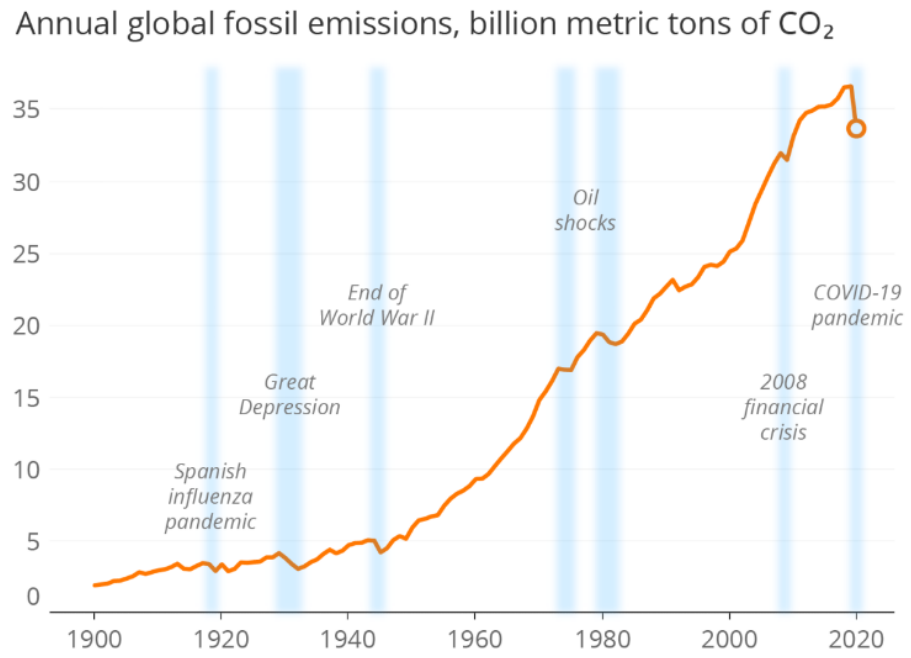

Figure 1.1: Annual global fossil emissions[12].

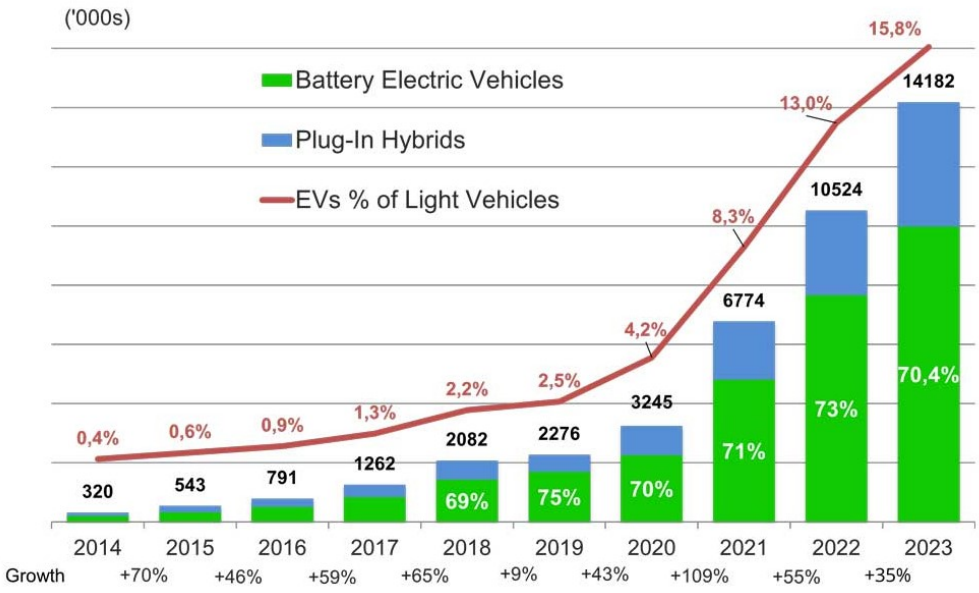

Figure 1.2: Growth in global electric vehicle transactions [4].

It is evident that since 2018, battery electric vehicles (BEVs) have consistently accounted for approximately 70% of annual EV sales. The market share of electric vehicles within the broader automotive industry has shown continuous growth, particularly between 2020 and 2024, underscoring the increasingly significant role that EVs are playing.

Figure 1.3 presents a forecast for EV sales over the next decade. Global EV sales are projected to triple, rising from 10.5 million units in 2022 to over 31 million by

2027, and are expected to more than double again, exceeding 74.5 million units by 2035. The number of EVs in operation is anticipated to increase rapidly. From 2024 onward, the adoption rate of plug-in EVs is projected to continue its steady ascent through 2033, with annual sales growth consistently exceeding 10%. This indicates that EVs will continue to exert a substantial impact in the coming decade.

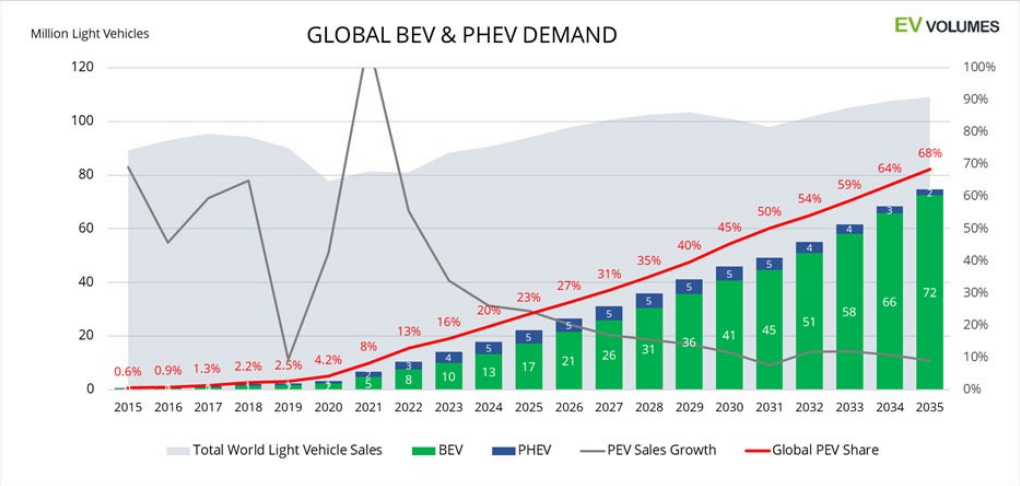

Figure 1.3: Forecast for EVs sales to 2035 [8].

Compared to internal combustion engine (ICE) vehicles, EVs still present certain challenges, as outlined in [21]. One significant issue is their impact on voltage stability. When EVs are connected to the distribution grid, they affect load dynamics and voltage distribution. The integration of EVs typically increases the load on distribution generators (DG) and decreases the voltage at various line nodes, with this effect being particularly severe at terminal nodes. Such voltage drops can disrupt the normal power supply to end users [22].

Additionally, the growing production and use of EVs have raised concerns about the disposal of retired batteries. Improper disposal can lead to environmental pollution [13], making battery recycling and reuse a priority. Batteries that retain only 70% of their capacity when fully charged are classified as second-life batteries (SLBs). Some researchers suggest that SLBs could be utilized in small DGs, where they could contribute to optimizing network infrastructure and improving the reliability, quality, and security of power supply [15]. Others propose using retired batteries in fast charging stations to reduce contracted grid power and mitigate disturbances [10]. The proposed structure is depicted in Figure 1.4 [3].

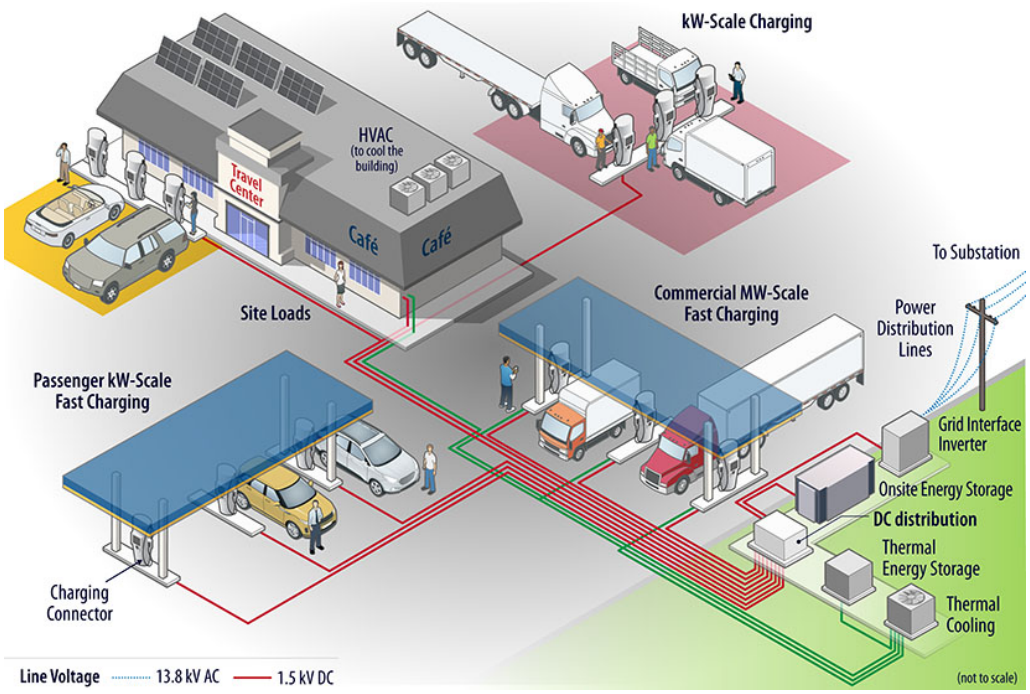

Figure 1.4: Structure of charging station.

Building on the points discussed above, as more electric vehicles (EVs) connect to the power grid for charging, the resulting increased load can lead to voltage fluctuations and the generation of harmonics. Integrating second-life batteries (SLBs) into fast charging stations offers a potential solution to mitigate these voltage instabilities and improve overall system efficiency. This thesis primarily aims to evaluate the feasibility of deploying SLBs in fast charging stations and to assess their performance in this context.

Additionally, due to varying degrees of degradation among SLBs, implementing an effective balancing strategy is crucial. A battery equalizer is an essential component in battery stacks, as differences in capacity between connected cells arise over time due to capacity fade and self-discharge. Without a battery equalizer, some cells may become overcharged while others remain undercharged during charging, and similarly, some cells may be under-discharged while others are over-discharged during discharging [2][16]. These imbalances can significantly reduce the overall efficiency of the battery pack and shorten its usable lifespan.

1.2 Motivation

To address the issues of grid voltage instability and uneven battery capacity, this study proposes a method to alleviate grid pressure by integrating second-life batteries (SLBs) into fast charging stations and employing battery equalizer technology to enhance the performance and lifespan of battery packs. This approach not only improves grid stability but also extends battery life and increases overall system efficiency. It is anticipated that the findings of this study will positively influence

the future development of power systems and electric vehicle technologies.

1.3 Objectives

The main objectives of the thesis are listed below:

- This thesis will select an appropriate equivalent circuit model for the battery to facilitate the analysis and identification of its parameters.
- The converter is designed to scale up the voltage, meeting the requirement of the power gird.
- The control strategy is also developed to stabilized the output voltage. Additionally, the load disturbance observer is designed to compensate for the overshoot/undershoot of the output voltage.
- A current allocation strategy is implemented to manage battery modules with varying levels of degradation and state of health (SoH). By balancing these differences, the strategy ensures that the battery pack operates effectively.

1.4 Outline

This thesis aims to address the application of SLBs in fast charging stations and is organized into three main sections. First, it will cover battery modeling, including the identification of internal resistance and capacitance parameters. Additionally, the development of the converter model and the associated control strategy will be discussed. Finally, the thesis will address the current allocation method for balancing battery packs.

Chapter 2 provides the foundational theory relevant to the thesis, covering battery modeling, DC/DC converter design, and SoH balancing. This chapter also includes the selection of the charging station topology.

Chapter 3 focuses on the construction of the thesis model. It begins with the development of the battery model and the principles of parameter identification. Next, the design of the DC/DC converter is detailed, with an emphasis on stabilizing output voltage through the application of a PI controller in the simulation model.

Chapter 4 focuses on the problem of voltage overshoot/undershoot of the converter. Additionally, one current allocation control strategy among different battery modules is introduced.

Chapter 5 presents the simulation results from the preceding chapters and provides an analysis of these results.

Chapter 6 concludes the thesis with a summary of findings and suggestions for future research.

2

Theoretical Fundamentals

This chapter presents all the theoretical foundations relevant to the thesis, with a particular focus on the equivalent circuit of batteries and DC/DC converter systems.

2.1 Introduction of Charging Stations

In this thesis, 12 battery cells which are connected in series, along with its associated converter, is defined as a battery modules. Multiple battery modules are then combined and integrated into the charging station. The system schematic is illustrated in Figure 2.1.

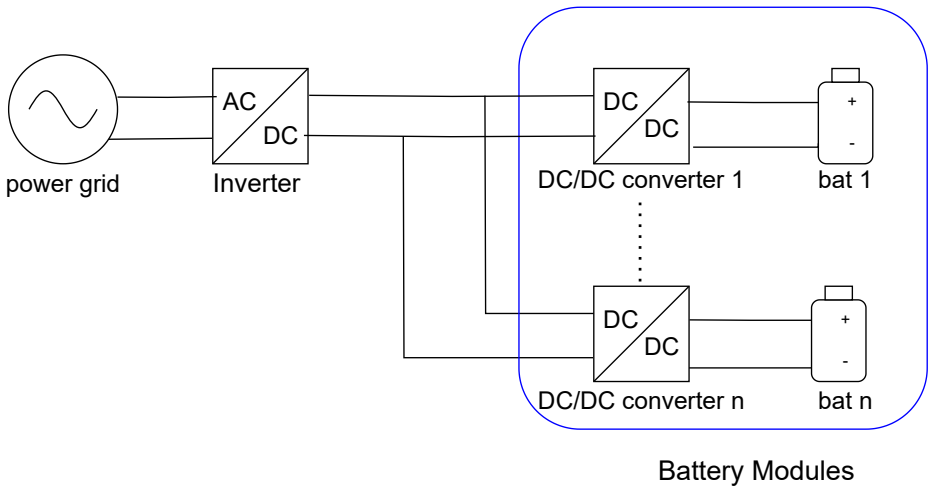

Figure 2.1: Structure of battery modules.

2.1.1 Features of Charging Stations

Since complete battery packages are employed in charging stations, it is essential to analyze the types of charging stations as well. Charging stations are generally categorized into two types: AC charging stations and DC charging stations.

Figure 2.2 depicts the typical system schematic of an AC charging station, which is directly connected to the AC power grid. This system is powered by medium-voltage AC (MVAC) and incorporates a battery energy storage system (BESS) to provide supplementary power during the charging process. Additionally, a line-frequency transformer (LFT) is employed to adjust the frequency, ensuring it meets the specifications required by the user terminal.

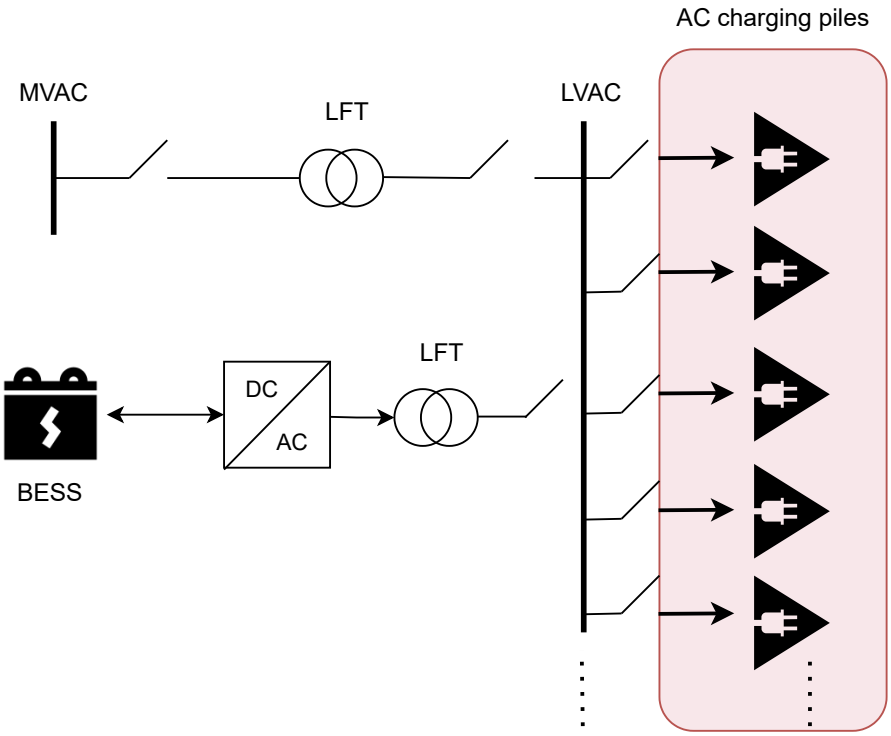

Figure 2.2: System structure of AC charging system.

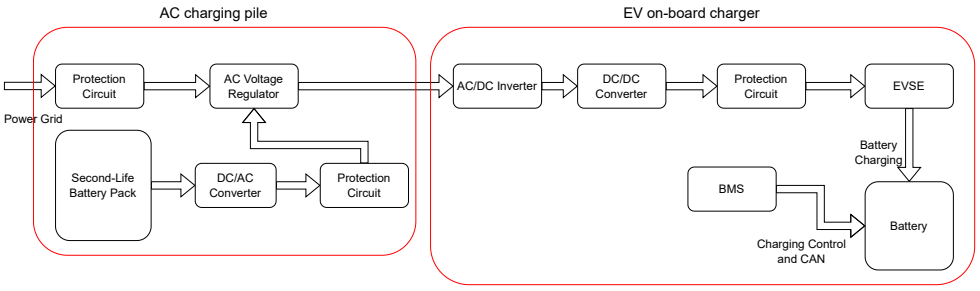

Figure 2.3: Structure of AC charging pile.

Figure 2.3 illustrates the structure of an AC charging station, which is directly powered by the grid. In Europe, conventional AC charging stations are categorized into

two levels. Level 1 operates at approximately 120V with currents ranging from 6A to 16A, depending on the battery capacity. Level 2 provides a fixed current of around 80A, with voltage varying between 208V and 240V to comply with regional voltage regulations. An on-board charger converts AC power to DC power for charging, following the SAE J1772 (2017) standards for single-phase AC charging. After drawing power from the grid, a converter adjusts the voltage to match the electric vehicle's requirements. The common charging approach involves delivering a constant current until a predetermined voltage is achieved, at which point a constant voltage is applied to complete the charging process. Charging is considered complete when the current drops to zero. Extensive research has been conducted on AC charging technology, including techniques to mitigate AC interference [9].

Different from the topology of AC charging stations, for the DC charging piles, the system structure is shown in Fig. 2.4.

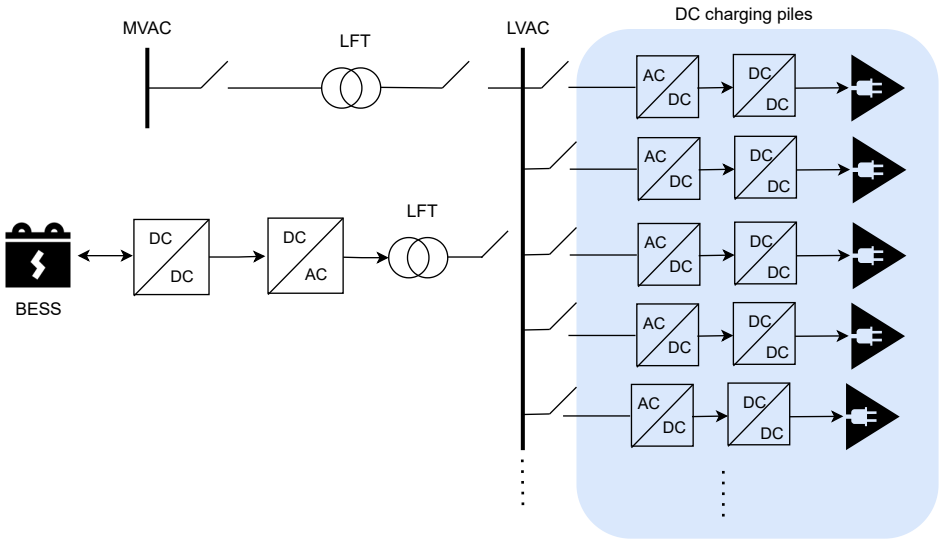

Figure 2.4: System structure of DC charging piles.

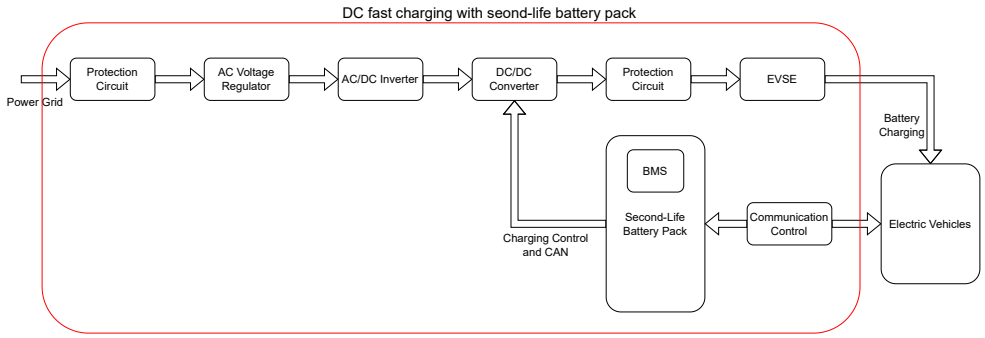

Figure 2.5: Structure of DC charging piles.

Figure 2.5 depicts the structure of a DC charging station. Unlike AC charging stations, DC charging stations have converters integrated directly into the charging piles. These converters adjust the voltage to meet the specific requirements of the electric vehicles (EVs), while a protection circuit prevents power from flowing back into the grid, thus avoiding potential disturbances [20]. Similar to AC charging, DC charging is categorized into two levels. Level 1 provides a current of 80A with a voltage range from 50V to 1000V, whereas Level 2 supports currents up to 400A while maintaining the same voltage range of 50V to 1000V.

2.1.2 Comparisons between AC and DC Charging Stations

Having provided a brief overview of AC and DC charging stations, it is important to highlight their respective advantages and disadvantages. Figure 2.6 illustrates these differences clearly. Notably, AC charging stations require on-board chargers to convert AC power to DC power, whereas DC charging stations can deliver power directly to the battery without the need for an on-board converter.

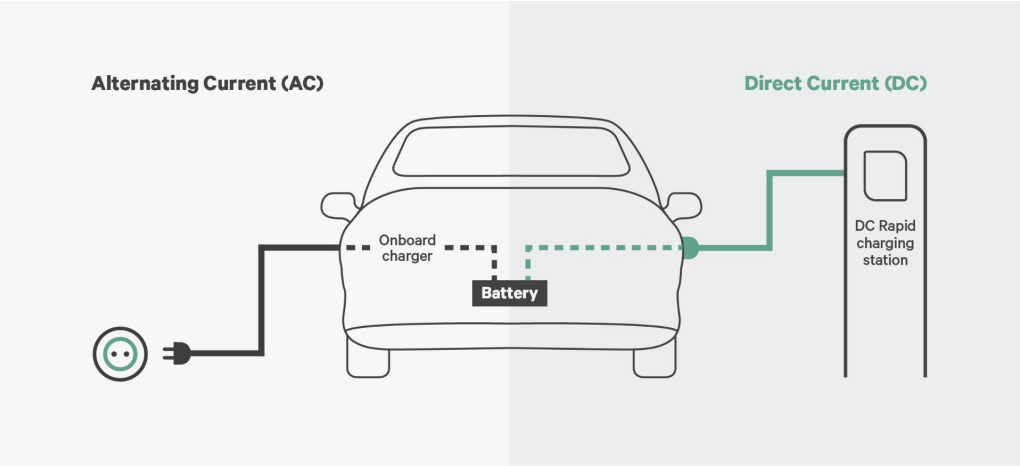

Figure 2.6: Comparison between AC and DC charging [19].

For the AC charging stations, the advantages are:

- Low cost for manufacturing.
- Easy construction.
- Relatively small load on the grid.
- The power distribution cabinets in the community can be directly installed.

The disadvantage is:

- Long charging time for the EVs.

For the DC charging stations, the advantages are:

- Short charging time for the EVs.

The drawbacks are:

- Complex installation.
- High demand for the community equipment.
- Large load on the transform.

Since this thesis focuses on battery applications in fast charging stations, the simulation utilizes the DC charging scenario due to its higher charging speed.

2.2 Battery Energy Storage System

2.2.1 Structure of Battery Systems

The configuration of the battery pack is crucial, as it is increasingly recognized in the energy storage market for its exceptional characteristics, including high specific and volumetric energy and power densities, charge/discharge efficiency, longevity, and overall performance [1]. Figure 2.7 illustrates the arrangement of batteries within charging piles and stations.

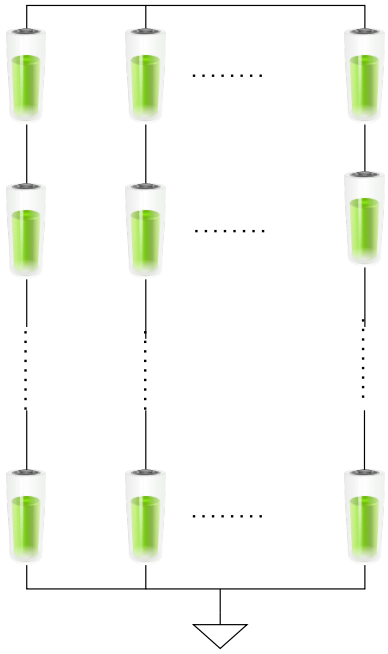

Figure 2.7: Series/Parallel connection of the battery cells.

When battery cells are connected in series, the open-circuit voltage (OCV) increases proportionally, as the individual cell voltages add up. For n cells, each with a voltage of V, the total voltage is $n \times V$. On the other hand, when cells are connected in parallel, the voltage remains constant, but the overall capacity of the module increases proportionally, since the parallel configuration boosts the total current supply. For m battery cells, each with a capacity of C, the total capacity becomes $m \times C$.

2.2.2 Equivalent Circuit Model

The equivalent circuit model of a battery is frequently employed to simulate its real-world behavior and to predict its performance. A typical battery equivalent circuit model comprises several components, including internal resistance, capacitance, and OCV. Internal resistance represents the battery's inherent resistance, which impacts voltage drop and efficiency during both charging and discharging. Capacitance reflects the battery's dynamic characteristics, such as its transient response, and can simulate voltage variations during the charging and discharging processes. More sophisticated models may incorporate multiple resistors and capacitors to enhance the accuracy of the simulation. For instance, series resistors and capacitors can replicate the internal resistance and charge storage properties of a battery. One of the most widely used equivalent circuit models is the Randles Circuit, as depicted in Figure 2.8.

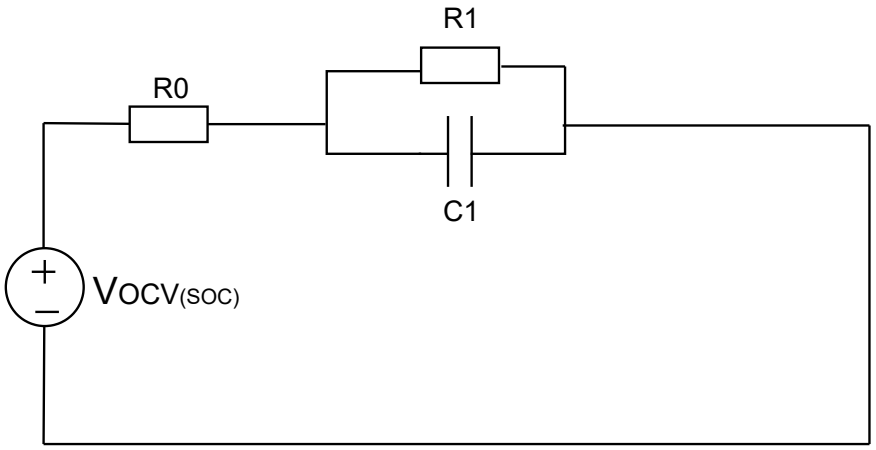

Figure 2.8: Schematic of Randle circuit.

Figure 2.8 illustrates the Randles Circuit, an equivalent circuit model consisting of two resistors and one capacitor. In this model, R_0 represents the solution resistance, which is the resistance of the electrolyte solution between the working electrode and the reference electrode. R_1 denotes the charge transfer resistance at the electrode-electrolyte interface, reflecting the kinetics of electrochemical reactions occurring there. C_1 represents the capacitance of the electrical double layer formed at the electrode-electrolyte interface due to charge separation.

In low-frequency tests, the charge transfer resistance R_1 and the double-layer capacitance C_1 predominantly influence the results. At high frequencies, the electrolyte resistance R_0 has the greatest impact. In the medium-frequency range, the results reflect a combination of R_1 and C_1. The second-order RC equivalent circuit model offers a more accurate description of the battery's non-linear characteristics. This model provides high estimation accuracy, is suitable for online applications, and has an acceptable computational load. Studies have shown that the second-order RC model can reduce the State of Charge (SoC) estimation error by 2.3%, whereas the first-order RC model results in an error of up to 6.2% [25][11]. This is why the second-order RC equivalent circuit is utilized in this thesis.

In addition to resistance and capacitance, the OCV is another crucial parameter in the Randles Circuit. OCV is influenced by the SoC of the battery, which indicates the remaining charge as a percentage of the total capacity. A SoC of 100% corresponds to a fully charged battery, while 0% indicates a completely discharged battery. The SoC provides an estimate of the battery's current energy level and is described by the equation 2.1.

$$SoC(t) = SoC(t_0) + \frac{1}{C_{nominal}} \int_{t_0}^{t} I(t)dt \tag{2.1}$$

In the SoC equation, $SoC(t_0)$ represents the initial State of Charge, $C_{nominal}$ is the

nominal battery capacity measured in ampere-hours (Ah), and $I(t)$ denotes the current at time t. The term $\int_{t_0}^{t} I(t)dt$ signifies the integral of the current over the period from t_0 to t, reflecting the change in battery capacity throughout the charging and discharging processes. While current integration is an effective method for dynamically tracking the battery's state of charge, it requires precise measurement and integration of the current.

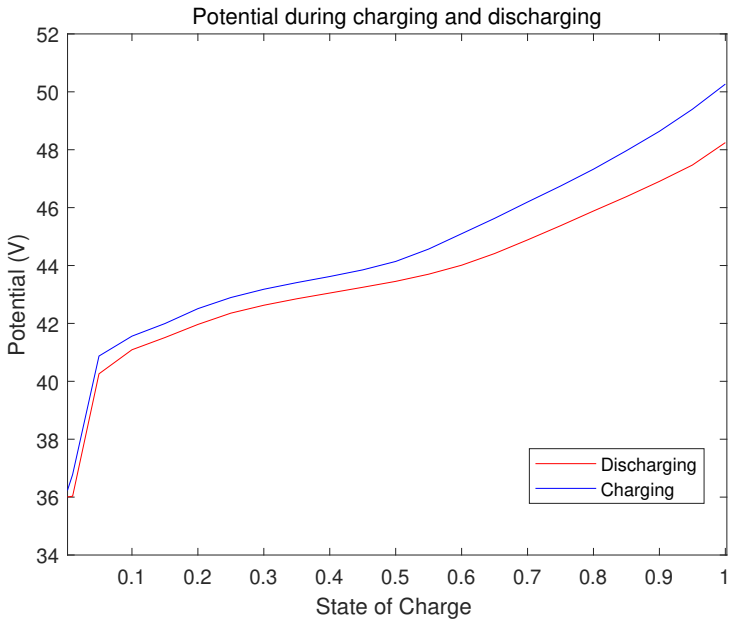

Figure 2.9: OCV model of the selected battery module.

As previously mentioned, the OCV is influenced by the SoC. The OCV of a battery is the voltage measured when the battery is not under load. Typically, OCV-SoC curves are derived from experimental data, which are obtained by measuring the OCV at various SoCs. These curves allow for the OCV at any given SoC to be determined through table lookup or interpolation. Figure 2.9 displays the OCV data for the selected battery modules provided by Volvo Energy. It is evident that the charging and discharging curves do not overlap due to variations in resistance during charging and discharging. However, for the purposes of battery parameter identification in this thesis, the charging data is utilized, as the voltages for charging and discharging are comparable under the same SoC conditions.

After extensive cycles of charging and discharging, a battery will inevitably undergo aging. The State of Health (SoH) is a crucial metric used to assess the battery's condition and degree of degradation. It is commonly expressed as a percentage, where 100% signifies the health of a new battery, and lower percentages indicate reduced capacity and performance. Equations 2.2 and 2.3 outline the methods for calculating SoH and the degree of degradation, respectively.

$$SoH = \frac{C_{Current}}{C_{Rated}} * 100\% \tag{2.2}$$

$$Degradation = 1 - SoH = 1 - \frac{C_{Current}}{C_{Rated}} * 100\% \tag{2.3}$$

$C_{Current}$ represents the current capacity, while C_{Rated} denotes the rated capacity of the battery. As a battery ages, its performance inevitably declines due to several factors, which can be broadly classified into chemical, mechanical, and thermal aspects. Over time, the electrolyte in the battery can decompose, producing gas and solid by-products that reduce ionic conductivity and impair the battery's ability to deliver current. Similarly, active materials in the electrodes can undergo irreversible changes; for instance, in lithium-ion batteries, the loss of lithium inventory and the growth of the solid electrolyte interphase layer on the anode can consume active lithium, thereby reducing capacity. Consequently, addressing the aging process is crucial in the analysis and development of battery technologies.

2.3 Power Electronics Converters

Since the battery cells are connected to DC/DC converter and modules can be connected in parallel to make up for the battery package which can be applied in the charging stations. It's also important to introduce the topology of the DC/DC converters.

2.3.1 Topology Overview

Managing the power flow among the several modules such as photo voltaic, wind, energy storage systems (ESS), battery, and the grid is a big challenging problem. In this regard, the implementation of DC-DC power converters are play a major role[6].The DC/DC converter is a type of power electronic device that converts one DC voltage into another DC voltage. There are many types of DC/DC converter topologies, each with its own specific advantages, disadvantages, and application scenarios. As shown in Figure 2.10, the DC/DC converter can be classified as Linear Mode, Hard Switching Mode and Soft Switching Mode. For the linear mode converter, they use linear elements (such as transistors or MOSFETs) to regulate the output voltage in their linear operating region. The input voltage is stepped down directly through the linear control element, and the output voltage is determined by the on-resistance of the control element and the load current. But the drawback is also obvious, since the efficiency is low. For the soft switching mode, complex control circuits are required to achieve soft switching, which is difficult to design and debug. So, the Hard Switching Mode Converter is decided to apply in this thesis.

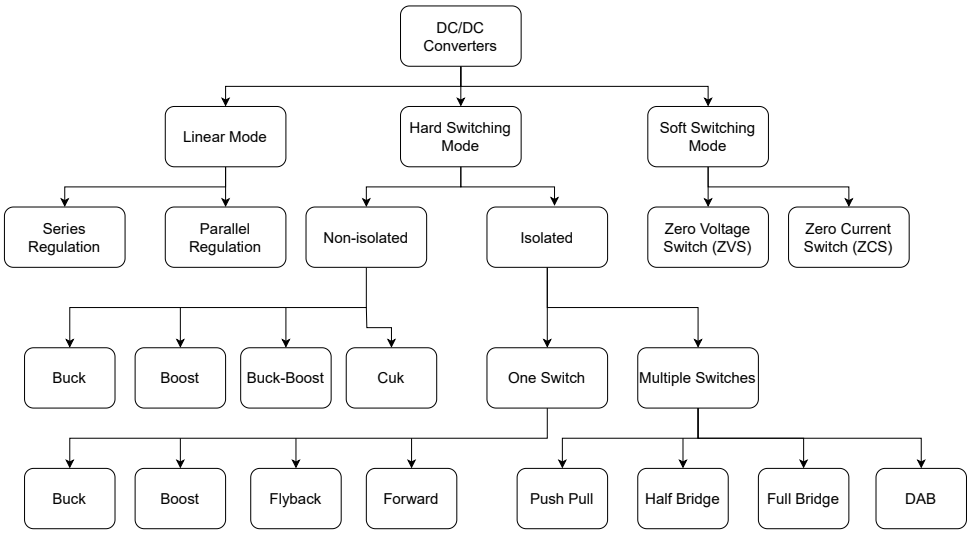

Figure 2.10: Classification of DC/DC converters [6].

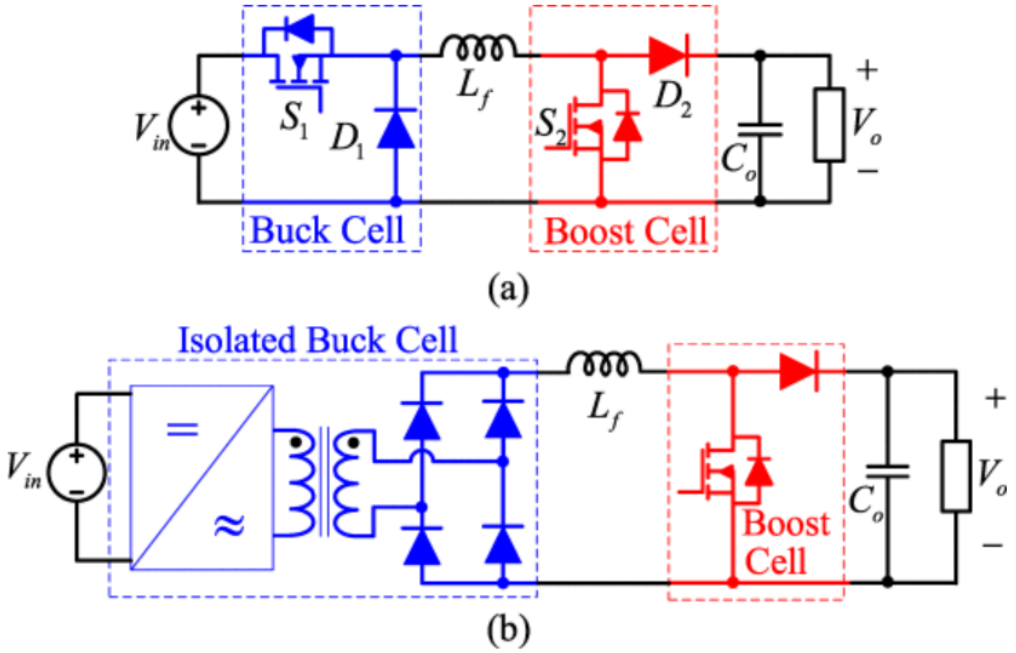

Figure 2.11: Topology of isolated and non-isolated converter.

The isolated topology offers electrical isolation between the input and output, thereby enhancing system safety. This isolation is crucial in high-voltage and high-power applications, as it protects output devices from high voltage or short circuits even if a fault occurs on the input side. However, the inclusion of isolation components, such as transformers, makes the circuit more complex and the design more challenging, as illustrated in Figure 2.11. Therefore, for the purposes of this thesis, a non-isolated topology has been chosen.

As illustrated in Figure 2.10, the non-isolated topology can be categorized into several types, including Buck Converter, Boost Converter, and Cuk Converter, among others. Given that the battery module used in this thesis must be capable of both charging and discharging, the Buck-Boost Converter is identified as the most suitable circuit for this application.

2.3.2 Operation Principle

The Buck-Boost converter is a DC-DC voltage converter capable of operating when the input voltage is higher, lower, or equal to the output voltage. It integrates the functions of both buck and boost converters, allowing it to efficiently convert the input voltage to the desired output voltage. The schematic of the Buck-Boost converter is shown in Figure 2.12.

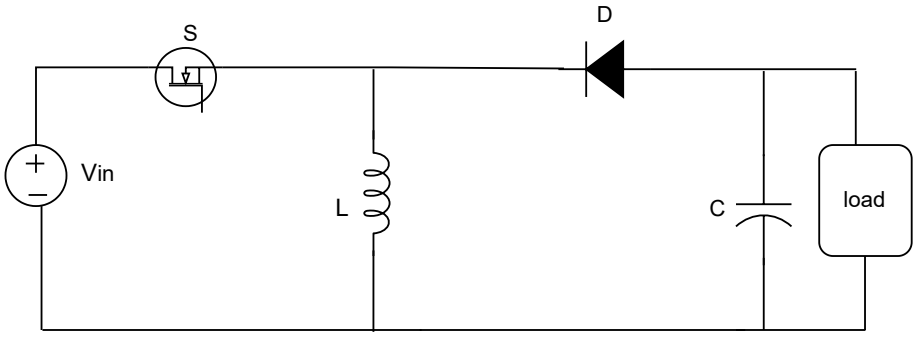

Figure 2.12: Schematic of buck-boost converter.

The Buck-Boost Converter operates in three primary modes: buck mode, boost mode, and buck-boost mode. When the input voltage is higher than the output voltage, the converter functions in buck mode. In this mode, when the switch is on, the inductor stores energy, and when the switch is off, the inductor discharges to the load through the freewheeling diode, thereby reducing the voltage. Conversely, when the input voltage is lower than the output voltage, the converter operates in boost mode. Here, the inductor stores energy while the switch is on, and upon turning off, the inductor releases energy, raising the output voltage through the diode.

When the input voltage is approximately equal to the output voltage, the converter smoothly transitions between buck and boost modes. The core principle of this converter is to regulate the output voltage by adjusting the switch's duty cycle. During the charging phase, when switch S is on, the current from the source flows through the inductor. Meanwhile, the capacitor C supplies energy to the load circuit through its discharge. The schematic of this operation is shown in Figure 2.13.

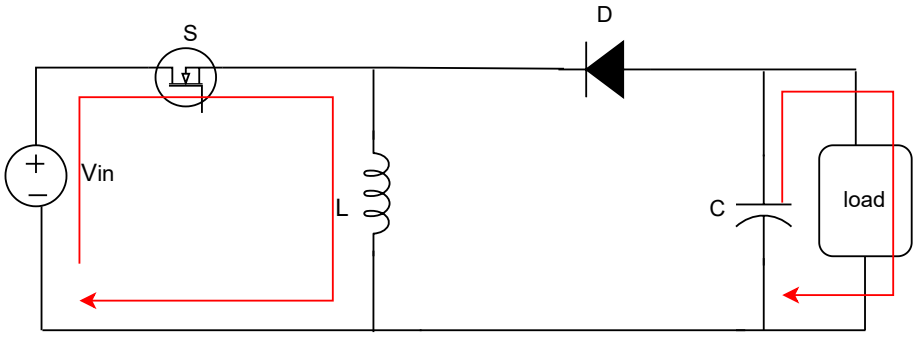

Figure 2.13: Buck-boost charging circuit.

During the discharging phase, the switch turns off. Due to the inductor's inability to change current instantaneously, it continues to supply power to the output capacitor C and the load via the diode D. This process ensures a steady flow of energy to the load even when the switch is inactive. The schematic for this operation is illustrated in Figure 2.14.

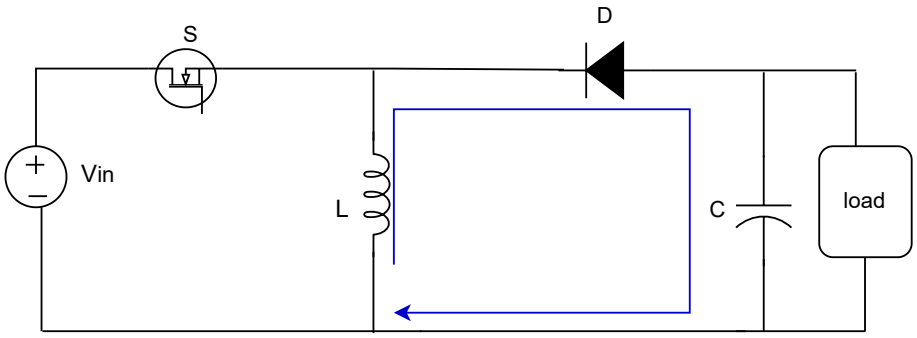

Figure 2.14: Buck-boost discharging circuit.

Combined these two modes together and assuming the power over the inductor is constant, the voltage equation can be listed below:

$$V_{in} * T_{on} = V_{out} * T_{off} \tag{2.4}$$

$$V_{in} * D * T = V_{out} * (1 - D) * T \tag{2.5}$$

$$V_{out} = \frac{D}{1 - D} * V_{in} \tag{2.6}$$

$$\Rightarrow D = \frac{V_{out}}{V_{in} + V_{out}} \tag{2.7}$$

In these equations, V_{in} represents the input voltage of battery terminal, V_{out} represents the output voltage of the load terminal, T_{on} is the conducting time during

charging, T_{off} is the time during discharging and D is the duty cycle. From Equations (2.6) and (2.7), it can be determined that if the duty cycle D is less than 0.5, the converter operates in buck mode. Conversely, if the duty cycle D is greater than 0.5, the converter functions in boost mode. However, these equations only account for the absolute value of the voltage and do not consider the direction of the output voltage.

To determine the inductance and capacitance values in the circuit, it is necessary to first calculate the current ripple I_{ripple}. Typically, the current ripple is assumed to be 30% of the sum of the input and output currents. During the switch's conduction phase, the voltage across the inductor equals the input voltage, allowing the inductance L to be calculated as follows:

$$L = \frac{D * V_{in}}{0.3 * F_{sw} * (I_{in} + I_{out})} \tag{2.8}$$

With the selected inductance, the peak current I_{peak} flowing through the inductor is:

$$I_{peak} = I_{in} + I_{out} + \frac{I_{ripple}}{2} \tag{2.9}$$

When calculating the capacitance, the voltage ripple V_{ripple} is one of the most important parameters for the calculation. Commonly, it depends on the design requirements or converter functionality. The equation for the capacitance can be written as where F_{sw} represents the switching frequency of the system:

$$C = \frac{(1 - D) * I_{in}}{V_{ripple} * F_{sw}} \tag{2.10}$$

2.3.3 Control Method

In DC/DC converters, the control method refers to the strategy used to control the switching elements (such as transistors) to regulate the output voltage or current. This technique is critical as it directly influences the converter's efficiency, performance, and ability to respond to changes in load or input voltage. Various modulation methods exist, with some being error-based, such as Proportional-Integral (PI) control[14], while others, like Model Predictive Control (MPC)[17], rely on mathematical models to solve an optimization problem in each control cycle to determine the appropriate control input.

For the PI control, It is mainly used in control systems that need to eliminate steady-state errors and do not require high system response speed. The advantages are:

- Easy to use: PI controller is simple in design, easy to understand and implement, and does not require complex mathematical models.
- Fast response: For many industrial applications, PI controllers can provide fast enough response speed to meet control requirements.

- Robustness: The PI controller has a certain degree of robustness to system parameter changes and external disturbances, and can maintain good control performance under a wide range of conditions.

The disadvantages are:

- Limited performance: PI controllers have limited performance when dealing with multi variable systems and constraints and cannot optimize overall system performance like MPC.
- Poor hysteresis handling: PI controllers may not perform as well as MPC when handling system delays and dynamic changes.

For the MPC control, its basic principle is to predict the future behavior of the system by building a mathematical model of the system, and adjust the control input in real time according to these prediction results to achieve the best control effect. The advantages are:

- Optimizing performance: MPC solves an optimization problem to determine the control inputs and can provide excellent control performance, especially in complex and multi variable systems.
- Multi variable control: Ability to handle multiple-input multiple-output systems and coordinate the interactions between variables

The disadvantages are:

- Computational complexity: Solving optimization problems in real time requires high computational resources, especially when the system is complex or the sampling rate is high.
- Model dependence: MPC depends on the accuracy of the system model, and model errors will affect the control effect.

From the analysis above, the thesis model requires the stable robustness and the fast response for the voltage stabilization. As a result, the PI control is selected in this thesis, rather than MPC control.

3

Modelling of Second-Life Batteries and DC/DC Converters

In Chapter 2, the theoretical foundations are established, including the Equivalent Circuit Model (ECM) for the battery and the topology for the DC/DC converter. Building on this groundwork, the current chapter introduces the thesis model. The battery is modeled using a second-order RC circuit, while a modified buck-boost converter topology is proposed for the DC/DC converter. Additionally, control strategies are developed to ensure a stable output voltage.

3.1 Battery Modelling and Parameter Identification

3.1.1 Equivalent Circuit Modelling

As previously discussed, to enhance the accuracy of the model and results, a second-order RC circuit is utilized in this thesis. This approach allows for the representation of both fast and slow response dynamics within the process. Figure 3.1 illustrates the second-order circuit employed in this study.

In this circuit, the currents flowing through R_0,R_1, C_1, R_2,and C_2 are denoted as i, i_1, i_2, i_3, and i_4. The open circuit voltage, $V_{OCV(SOC)}$ varies with the state of charge (SoC), and V represents the model's output voltage. The RC branch is split into two components: one responsible for the fast response and the other for the slow response. R_0 accounts for the battery's polarization effects. The remaining task involves curve fitting to ensure that the simulated voltage closely matches the measured voltage. This is achieved using difference equations, a mathematical tool used to describe the dynamic behavior of discrete-time systems. Similar to differential equations, difference equations address values at discrete time points rather than continuous rates of change over time, making them useful for describing patterns of change in iterative processes or recursive relationships.

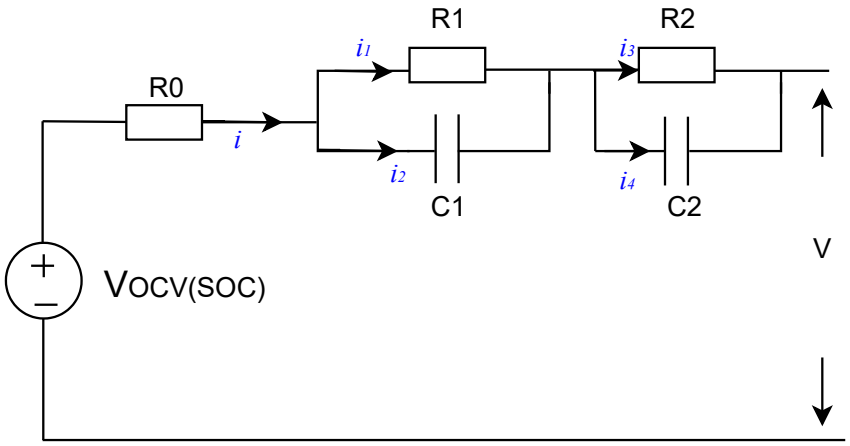

Figure 3.1: Equivalent circuit of the battery model.

3.1.2 Parameter Identification

Using the circuit shown in Figure 3.1, the voltage and current equations can be derived by applying Kirchhoff's laws as follows:

$$V = R_0 * i + R_1 * i_1 + R_2 * i_3 \tag{3.1}$$

$$i_1 = i - C_1 * \frac{d(i_1 * R_1)}{dt} \tag{3.2}$$

$$i_3 = i - C_2 * \frac{d(i_3 * R_2)}{dt} \tag{3.3}$$

However, one variable remains unknown: the open-circuit voltage (OCV). Fortunately, Volvo has provided data on the battery that allows us to plot the relationship between the state of charge (SOC) and the OCV. This means that once the SOC is determined, the OCV can be readily identified. A robust method to determine SOC is the ampere-hour method, which utilizes the rated capacity and current. The current data, provided by Volvo, serves as the input signal for the model. The equation for the ampere-hour method is given below:

$$SOC(t) = SOC(0) - \frac{1}{C_{rate}} \int i dt \tag{3.4}$$

C_{rate} stands for the rated capacity of the battery.
Additionally, the equation 3.1 3.2 3.3 are required to be simplified so that they can be applied in the Matlab. The matrix can be written as:

$$\begin{bmatrix} \frac{di_1}{dt} \\ \frac{di_3}{dt} \end{bmatrix} = \begin{bmatrix} -\frac{1}{C_1 * R_1} & 0 \\ 0 & -\frac{1}{C_2 * R_2} \end{bmatrix} \begin{bmatrix} i_1 \\ i_3 \end{bmatrix} + \begin{bmatrix} \frac{1}{C_1 * R_1} \\ \frac{1}{C_2 * R_2} \end{bmatrix} i \tag{3.5}$$

And then the matrix can be simplified,

$$\frac{di_1}{dt} = \frac{i_1(\Delta T) - i_1(0)}{\Delta T} = [-\frac{1}{C_1 * R_1} * i_1(0) + \frac{1}{C_1 * R_1} * i(0)] \tag{3.6}$$

$$\frac{di_3}{dt} = \frac{i_3(\Delta T) - i_3(0)}{\Delta T} = [-\frac{1}{C_2 * R_2} * i_3(0) + \frac{1}{C_2 * R_2} * i(0)] \tag{3.7}$$

So, current i_1 and i_3 can be known, which can be used in Matlab:

$$i_1(\Delta T) = [-\frac{1}{C_1 * R_1} * i_1(0) + \frac{1}{C_1 * R_1} * i(0)] * \Delta T + i_1(0) \tag{3.8}$$

$$i_3(\Delta T) = [-\frac{1}{C_2 * R_2} * i_3(0) + \frac{1}{C_2 * R_2} * i(0)] * \Delta T + i_3(0) \tag{3.9}$$

Moreover, during simulations in MATLAB, issues such as non-physical values for impedance components—such as negative resistance and capacitance—can arise. To address these issues and ensure accuracy, it is essential to impose constraints on the values. In this study, the approach employed involves minimizing the discrepancy between the simulation results and experimental measurements. The equation used for this optimization is provided below:

$$F(t) = \Sigma[V_{est}(t) - V(t)]^2 \tag{3.10}$$

Meanwhile, adding some boundary conditions can also help avoid the negative values:

$$R_{0lb} \leq R_0 \leq R_{0ub} \tag{3.11}$$

$$R_{1lb} \leq R_1 \leq R_{1ub} \tag{3.12}$$

$$R_{2lb} \leq R_2 \leq R_{2ub} \tag{3.13}$$

$$C_{1lb} \leq C_1 \leq C_{1ub} \tag{3.14}$$

$$C_{2lb} \leq C_2 \leq C_{2ub} \tag{3.15}$$

3.2 Buck-Boost Converter Modelling

In this section, the converter topology utilized is introduced, along with a detailed explanation of the component selection and control strategy. Building on the discussion in Chapter 2, the directional buck-boost converter has been chosen to meet the requirements for both charging and discharging. The topology of this converter is illustrated in Figure 3.2.

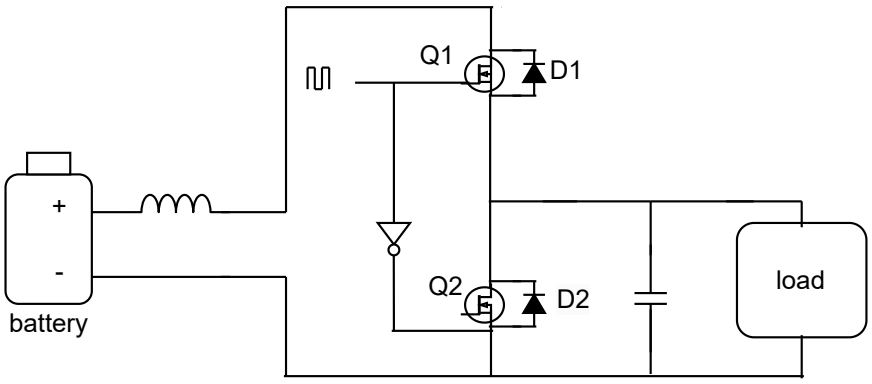

Figure 3.2: Topology of the battery circuit.

In boost mode, the switch Q2 and diode D1 are activated according to the duty cycle, while switch Q1 and diode D2 remain off throughout the operation. This mode can be further categorized into two intervals based on the conduction states of switch Q1 and diode D2 [18].

Interval 1 (Q2 on, Q1 off, D1 off, D2 off) : During this interval, the input voltage charges the inductor, causing the inductor current to increase continuously. Additionally, because diode D1 is reverse-biased and switch Q1 is off, no current flows through switch Q1.

Interval 2 (Q2 off, Q1 off, D1 off, D2 on) : During this interval, the current through the inductor cannot change instantaneously, leading to a reversal in the polarity of the voltage across it. Consequently, the inductor acts in series with the input voltage. This reversal forward-biases diode D1, allowing the inductor current to charge the output capacitor C2 to a higher voltage. As a result, the output voltage increases, achieving a "boost" effect.

3.2.1 Parameter Design

In this section, the inductance and capacitance values for the converter are calculated. Equations 2.4 to 2.10 describe the calculation methods for these components. Since the charge and discharge currents through the inductor must be equal, these equations are derived using Kirchhoff's Circuit Laws. The nominal voltage for the power grid is approximately 800V, which is also considered the ideal output voltage for the simulation. Additionally, the specifications for the circuit are provided by Volvo and are listed below:

$$V_{out} = \frac{V_{in}}{1 - D} \tag{3.16}$$

$$R = \frac{V_{out}^2}{P} \tag{3.17}$$

$$L_{min} = \frac{D * (1-D)^2 * R}{2f} \tag{3.18}$$

$$C_{min} = \frac{D * V_{out}}{R * f * V_{ripple}} \tag{3.19}$$

In this equations, D stands for the duty cycle, representing the conducting time ratio for the up gate in the circuit. V_{out} represents for the output voltage, V_{in} for the input voltage,R for the load resistance, f for the switching frequency and V_{ripple} for the voltage ripple.

When selecting parameters, it is important to incorporate a margin of 1.2 to 1.3 times the calculated values to account for practical variations. The relevant equations are provided below:

$$1.2 * L_{min} \leq L \leq 1.3 * L_{min} \tag{3.20}$$

$$1.2 * C_{min} \leq C \leq 1.3 * C_{min} \tag{3.21}$$

3.2.2 Transfer Function of Buck-Boost Converter

To gain a deeper understanding of the DC/DC converter, it is crucial to analyze the converter's transfer function. By applying Kirchhoff's law, the equations governing the inductor and capacitor can be readily derived.

During the charging time, the equations are:

$$L * \frac{di}{dt} = V_s * DT_{sw} \tag{3.22}$$

$$C * \frac{dV_{out}}{dt} = -\frac{V_{out}}{R} \tag{3.23}$$

And during the time DT_{sw}-T, the equation are:

$$L * \frac{di_L}{dt} = V_s - V_{out} \tag{3.24}$$

$$C * \frac{dV_{out}}{dt} = i_L - \frac{V_{out}}{R} \tag{3.25}$$

By integrating these equations, the equation over the inductor can be yielded:

$$\begin{aligned} \int_0^{T_{sw}} L\frac{di_L}{dt}dt &= \int_0^{dT_{sw}} V_s dt + \int_{dT_{sw}}^{T_{sw}} (V_s - V_{out})dt \\ \Rightarrow L\frac{di_L}{dt} \approx L\frac{\Delta i_L}{\Delta t} &= V_s - (1-d)V_{out} \end{aligned} \tag{3.26}$$

For the capacitor, it's also easy to get:

$$\begin{aligned} \int_0^{T_{sw}} C\frac{dV_{out}}{dt}dt &= \int_0^{dT_{sw}} -\frac{V_{out}}{R_L}dt + \int_{dT_{sw}}^{T_{sw}} (i_L - \frac{V_{out}}{R_L})dt \\ \Rightarrow C\frac{dV_{oout}}{dt} \approx C\frac{\Delta V_{out}}{\Delta t} &= -\frac{V_{oou}}{R_L} + (1-d)i_L \end{aligned} \tag{3.27}$$

3.2.3 Transfer Function of Control Loops

Moreover, to achieve a stable output voltage, it is important to derive the transfer function for the control system. This transfer function is essential for determining the parameters of the PI controller. In this analysis, the small-signal model is employed, leading to the necessary equations.

$$\begin{cases} v_{out} = V_{out} + \tilde{v}_{out} \\ d = D + \tilde{d} \\ i_L = I_L + \tilde{i}_L \end{cases} \tag{3.28}$$

In those equations, V_{out}, d and i_L respectively stands for output voltage, duty cycle and inductor current. The terms $\tilde{v}_{out}$, $\tilde{d}$, and $\tilde{i}_L$ represent the small signal variations.

By replacing the variables from small signal model:

$$\begin{cases} L\dfrac{d\tilde{i}_L}{dt} = -(1-D)\tilde{v}_{out} + V_{out}\tilde{d} \\ C\dfrac{d\tilde{v}_{out}}{dt} = -\dfrac{\tilde{v}_{out}}{R_L} + (1-D)\tilde{i}_L - \dfrac{V_{out}}{(1-D)R_L}\tilde{d} \end{cases} \tag{3.29}$$

By applying Laplace transform, the equations in frequency domain can be reached:

$$\begin{cases} sL\tilde{i}_L = -(1-D)\tilde{v}_{out} + V_{out}\tilde{d} \\ sC\tilde{v}_{out} = -\dfrac{\tilde{v}_{out}}{R_L} + (1-D)\tilde{i}_L - \dfrac{V_{out}}{(1-D)R_L}\tilde{d} \end{cases} \tag{3.30}$$

The diagram of the current controller is shown below:

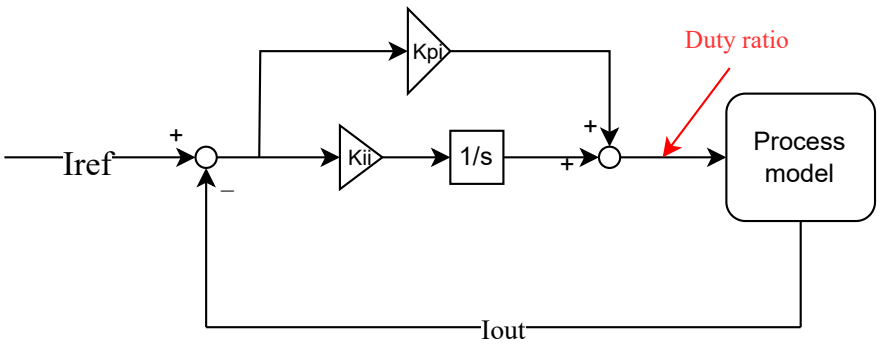

Figure 3.3: Topology of the current PI controller.

In this figure, the process model represents the circuit in MATLAB, I_{out} denotes the output current in the circuit model, and I_{ref} is the reference value for the output current. To design an effective current controller, the first step is to derive the open-loop equation for the controller, which can be readily obtained from Equation :

$$G_{id} = \frac{V_{out}CRs + 2V_{out}s}{CLRs^2 + Ls + R(1-D)^2} \tag{3.31}$$

Given that the open-loop system is a second-order system, which is somewhat complex and may lack stability, it is essential to simplify the system. The simplified system can be represented by the following equation:

$$G_{sid} = \frac{V_s}{L(1-D)s} \tag{3.32}$$

By plotting the Bode diagram around the frequency of the current controller, it is observed that in the high-frequency region, the simplified model aligns well with the model derived from the equation:

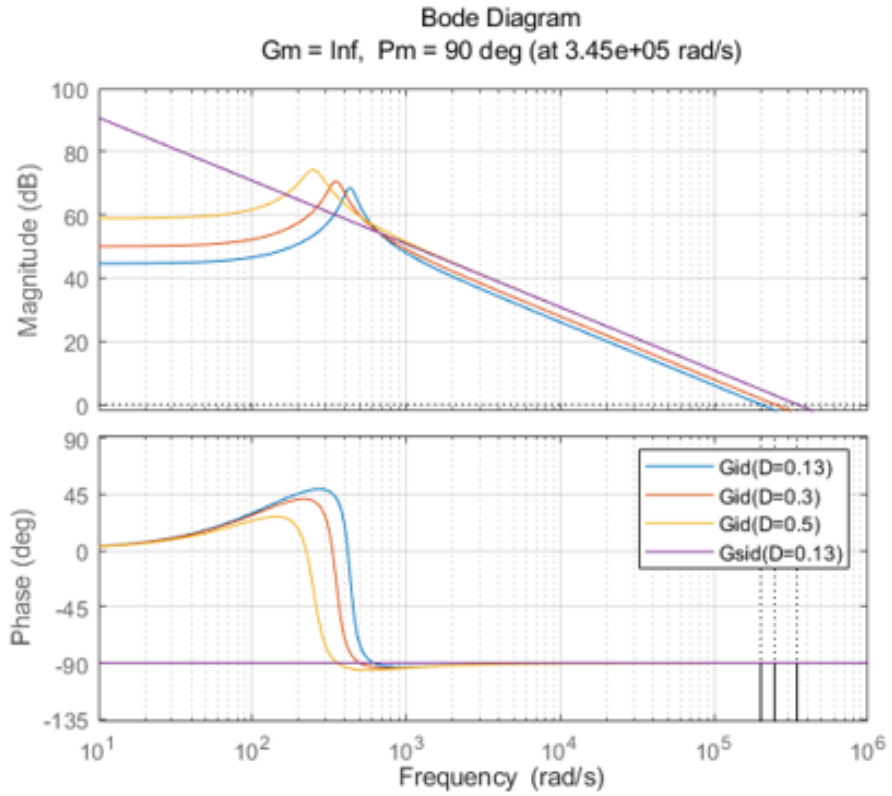

Figure 3.4: Comparison between original and simplified model.

Since the simplified model will be utilized in this thesis, the next step is to design the PI parameters in F_c for the current controller, which will be used to tune the system's bandwidth. The calculations are as follows:

$$\begin{aligned} &20\log_{10}(|G_c(s)|_{f=f_c}) = 20\log_{10}(|F_c(s)H_c(s)|_{f=f_C}) = 0 \\ \Rightarrow &20\log_{10}(|F_c(s)|_{f=f_C}) = -20\log_{10}(|H_c(s)|_{f=f_c}) = -28 \\ \Rightarrow &20\log_{10}(\sqrt{k_{cp}^2 + \frac{k_{ci}^2}{(2\pi f_c)^2}}) = -28 \end{aligned} \tag{3.33}$$

$$\begin{aligned} &\angle(G_c(s)|_{f=f_C}) = \angle(F_c(s)H_c(s)|_{f=f_C}) = -180^\circ + \phi_m \\ \Rightarrow &\angle(F_c(s)|_{f=f_C}) + \angle(H_c(s)|_{f=f_C}) = -180^\circ + \phi_m \\ \Rightarrow &\angle(F_c(s)|_{f=f_C}) = -90 + \phi_m \\ \Rightarrow &\frac{-k_{ci}}{2\pi f_c k_{cp}} = \tan(-90^\circ + \phi_m) \end{aligned} \tag{3.34}$$

As a result, the K_{cp} and K_{ci} value can be known:

$$\begin{cases} k_{cp} = 0.0434 \\ k_{ci} = 314.9 \end{cases} \tag{3.35}$$

The Bode diagram is a valuable tool for assessing the stability of the controller. The Bode diagram is shown in Figure 3.5:

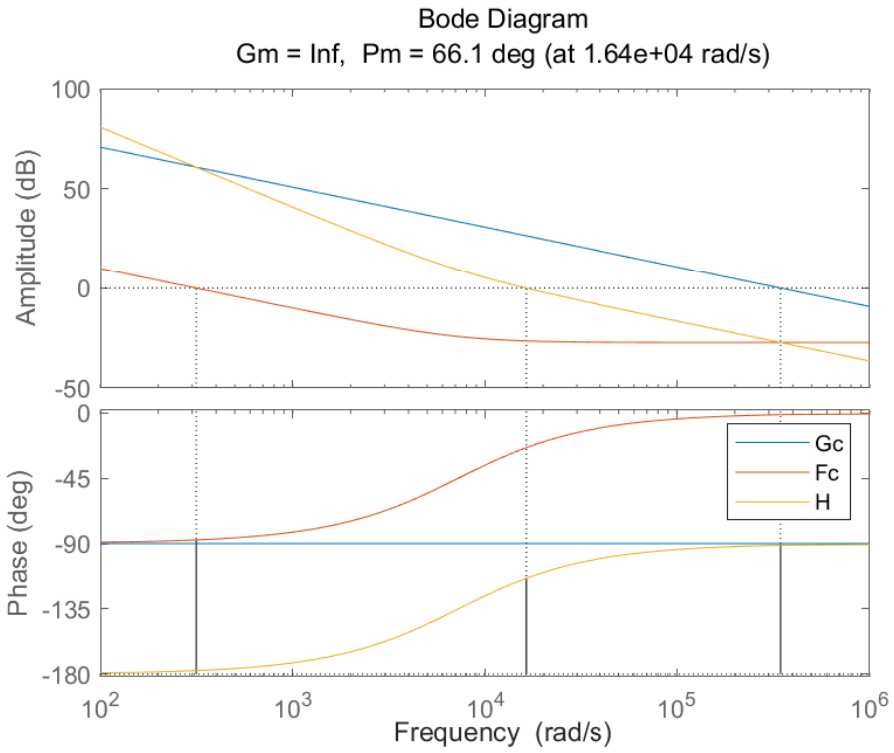

Figure 3.5: Bode diagram for the current controller.

In the figure above, H represents the open-loop function of the current controller, F_c denotes the controller's control function, and G_c represents the closed-loop function. It is evident that the amplitudes around the frequency are below the 0 dB line, indicating that the signals are gradually attenuating, while the phases remain above the -180 degree line. These two indicators confirm that the system is stable.

After designing the current controller, the same procedures can be applied to calculate the parameters for voltage control. First, the open-loop equation for the voltage controller can be derived:

$$H_v = \frac{-Ls + R(1-D)^2}{RC(1-D)s + 2(1-D)} \tag{3.36}$$

By plotting the Bode diagram for H_v, the corresponding amplitude and phase can be determined, allowing for the calculation of the voltage PI controller parameters:

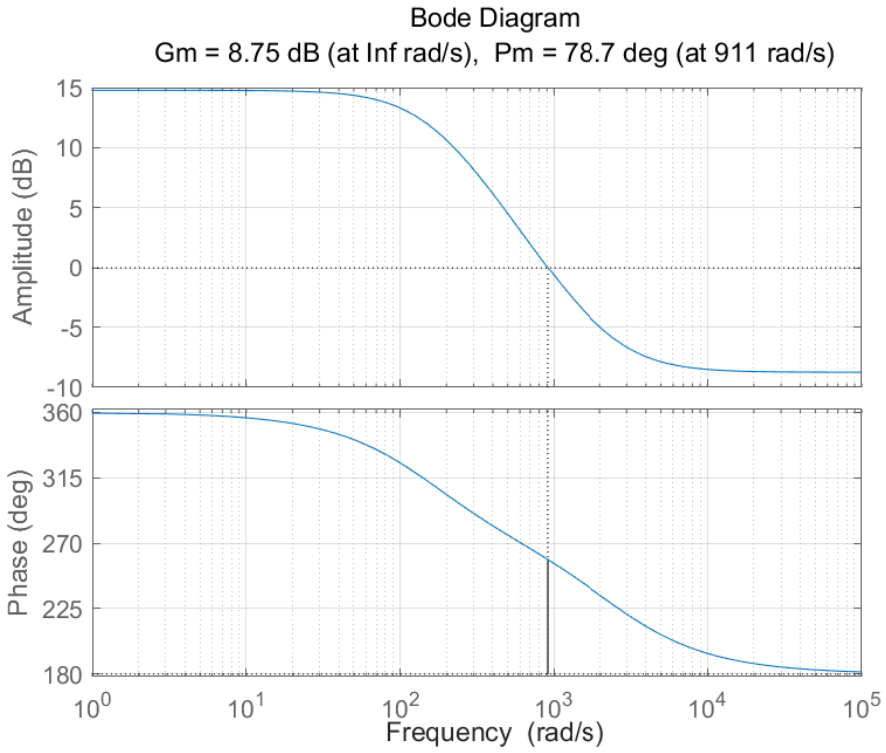

Figure 3.6: Bode diagram for voltage controller.

As shown in the figure above, a frequency of around 100 Hz can be selected, resulting in an amplitude of approximately 14. The corresponding equation is as follows:

$$\begin{aligned} &20\log_{10}(|G_c(s)|_{f=f_c}) = 20\log_{10}(|F_c(s)H_c(s)|_{f=f_C}) = 0 \\ \Rightarrow &20\log_{10}(|F_c(s)|_{f=f_C}) = -20\log_{10}(|H_c(s)|_{f=f_c}) = -14 \\ \Rightarrow &20\log_{10}(\sqrt{k_{cp}^2 + \frac{k_{ci}^2}{(2\pi f_c)^2}}) = -14 \end{aligned} \tag{3.37}$$

$$\begin{aligned} &\angle(G_c(s)|_{f=f_C}) = \angle(F_c(s)H_c(s)|_{f=f_C}) = -180° + \phi_m \\ \Rightarrow &\angle(F_c(s)|_{f=f_C}) + \angle(H_c(s)|_{f=f_C}) = -180° + \phi_m \\ \Rightarrow &\angle(F_c(s)|_{f=f_C}) = -90 + \phi_m \\ \Rightarrow &\frac{-k_{ci}}{2\pi f_c k_{cp}} = \tan(-90° + \phi_m) \end{aligned} \tag{3.38}$$

As a result, the values of K_vp and K_vi can be yielded:

$$\begin{cases} k_{vp} = 0.1728 \\ k_{vi} = 3.1342 \end{cases} \tag{3.39}$$

Furthermore, the stability of the voltage controller also matters to the whole system. The Bode diagram is shown in Figure 3.7 which can help judge whether is stable or not:

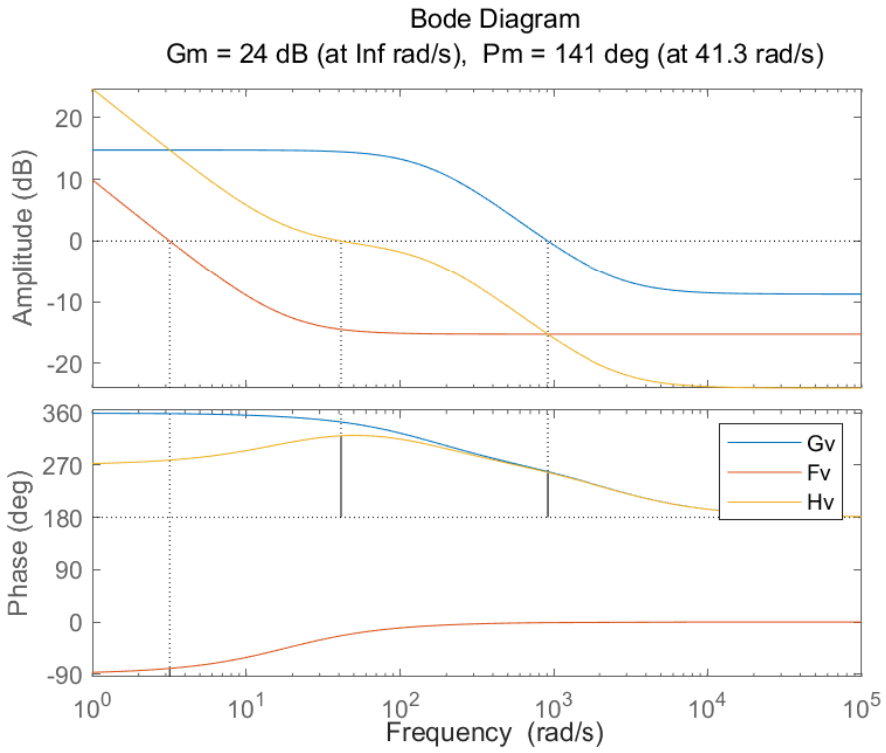

Figure 3.7: Bode plot for voltage system.

The block diagram of the voltage controller is shown in Figure 3.8:

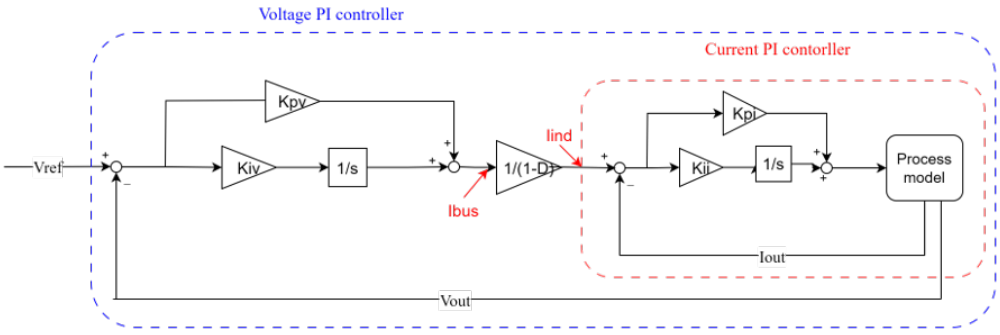

Figure 3.8: PI controller of the converter.

Similar to the current controller, both the amplitude and phase indicate the stability of the system. This means that the voltage and current controllers can be combined and applied in the simulation.

4

Voltage Fluctuation Suppression and Integration Control for Battery Packs

4.1 Integration of Battery Packs via Buck-Boost Converters

In the initial simulations, each battery module is paired with its own DC/DC converter and load circuit. When two modules are connected, they share a single load circuit and operate together with the SoH estimation loop. Due to variations in output power, the reference current must be adjusted accordingly. The structural changes are illustrated in Figure 4.1.

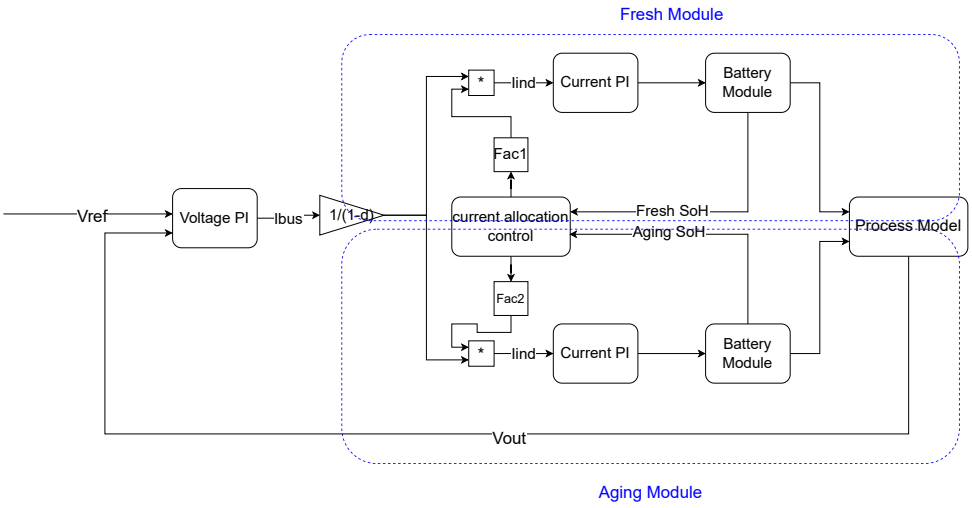

Figure 4.1: Structure of current allocation control.

4.1.1 Feed-Forward Compensator

Since the rise time of the output voltage is somewhat lengthy, the compensation loop should be designed to compensation for hysteresis in the voltage control loop. This

involves introducing a negative margin into the loop to counterbalance the original response. To accomplish this, a disturbance observer needs to be designed first. The principle schematic for this is shown in Figure 4.2.

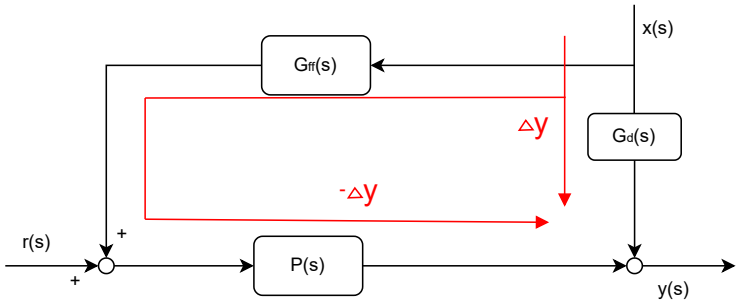

Figure 4.2: Schematic of compensation.

In this figure, $r(s)$ is the input signal of the whole system, which is the output voltage. $P(s)$ is the process model, including the PI controller and the circuit, $G_d(s)$ is the functions related to the bus capacitor, and the $G_{ff}(s)$ is the filter required to be designed[23]. The detailed schematic diagram is shown in Figure 4.2.

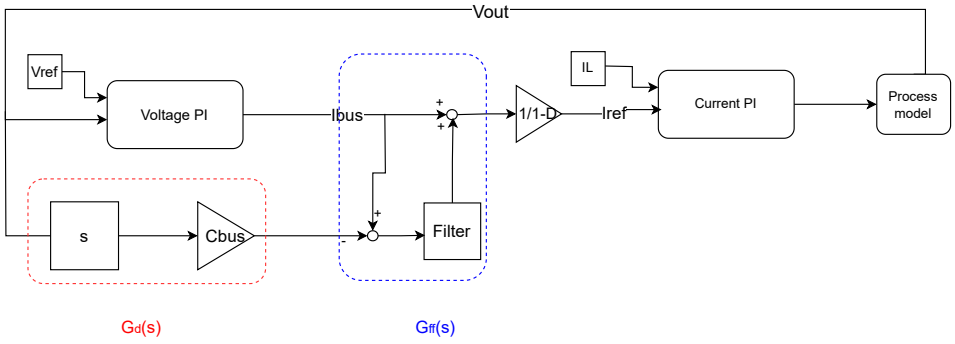

Figure 4.3: Schematic of Voltage Compensation.

4.1.2 Load Disturbance Observer

For the filter component in the loop, both first-order and second-order systems can be utilized. When designing the first-order system, the standard form is $\frac{1}{ks+1}$,requiring only the calculation of the parameter k. Considering the frequency of the voltage controller, the parameter can be designed as $k = 2 * pi/20000$. When designing the second-order system, in addition to the controller calculations, we only need to incorporate the error and compensation components.

$$\frac{dV_{out}}{dt} = a * i_L + F_1 * \delta_1 \tag{4.1}$$

$$\frac{di_L}{dt} = buV_{out} + F_2 * \delta_2 + \psi \tag{4.2}$$

In these equations, a equals to $\frac{1}{C}$, b equals to $-\frac{1}{L}$, u equals to 1-d, F_1 equals to $-\frac{1}{C}$, F_2 equals to $\frac{1}{L}$, and ψ equals to $\frac{V_i}{L}$. With equal (3.25) and (3.26), the state equation is easy to set:

$$\dot{x} = f(x) + g(x) * u + F\delta \tag{4.3}$$

$$Y = H(x) \tag{4.4}$$

And x=

$$\begin{bmatrix} x_1 \\ x_2 \end{bmatrix}$$

f(x)=

$$\begin{bmatrix} a * x_2 \\ \psi \end{bmatrix}$$

g(x)=

$$\begin{bmatrix} 0 \\ b * x_1 \end{bmatrix}$$

δ=

$$\begin{bmatrix} \delta_1 \\ \delta_2 \end{bmatrix}$$

F=

$$\begin{bmatrix} F_1 & 0 \\ 0 & F_2 \end{bmatrix}$$

After the simplification and calculations, the equations can be yielded:

$$s^2 + k_1 s + k_0 = 0 \tag{4.5}$$

$$k_0 * e - k_1 * \dot{y} - \ddot{\mathrm{y}} = -F_1 * \dot{\delta}_1 \tag{4.6}$$

$$H(s) = \frac{k_0}{s^2 + k_1 s + k_0} = \frac{w_n^2}{s^2 + 2\xi w_n s + w_n^2} \tag{4.7}$$

And in these equations, $k_1 = 2\xi w_n$ and $k_0 = w_n^2$.

"In a second-order system, ξ is typically set to approximately 0.707. Considering the rise time, the relationship between the rise time and these parameters is given by $t_s = 4/\xi w_n$. However, a shorter rise time results in larger ripples observed by the observer. Consequently, a rise time of 1 ms is selected.Once the filter is designed, it is important to verify the system's stability. The first step is to calculate the transfer function. Using Figure 3.8, the calculation can be performed as follows:

$$i_{bus} = I_{bus} + \Delta i_{bus} * G_2 \tag{4.8}$$

$$i_{bus} = (V_{oref} - V_{out}) * G1 + [i_{bus} * C_{bus2} - V_{out} * C_{bus}s] * G_2 \tag{4.9}$$

$$i_{bus} = G_1 * V_{oref} - G_1 * V_{oref} + i_{bus}C_{bus2}G_2 - V_{out}C_{bus}G_2s \tag{4.10}$$

$$i_{bus} = \frac{G_1 * V_{oref}}{1 - C_{bus2}G_2} \tag{4.11}$$

Finally, the transfer function can be set as:

$$\frac{i_{bus}}{V_{oref}} = \frac{G_1 * V_{oref}}{1 - C_{bus2}G_2} \tag{4.12}$$

In these equations, G1 is the voltage controller. s represents the differential part and C_{bus} stands for the bus capacitor at the output side. G2 is the designed filter, and $C_{bus}2$ is the reciprocal of C_{bus}.
So that G_1 can be written as:

$$G_1 = k_{pv} + \frac{k_{iv}}{s} = \frac{1.036s + 6.26}{s} \tag{4.13}$$

And when G_2 is the second order filter, it can be written as:

$$G_2 = \frac{2000598}{s^2 + 2000s + 2000598} \tag{4.14}$$

Totally, the transfer function can be written as:

$$\frac{i_{bus}}{V_{oref}} = \frac{1.0362 + \frac{6.26}{s}}{1 - \frac{2000598}{s^2+2000s+2000598}} \tag{4.15}$$

4.2 Current Allocation Control

As mentioned earlier, the integration of the battery module has been completed. Next, the fresh module and the aging module will be connected. The first step in this process is to develop the State of Health (SoH) estimation system.

4.2.1 SoH estimation

Since the two battery modules have different states of health, it is crucial to monitor their health values continuously, which is also important for effective balance control. The method for developing a State of Health (SoH) estimation model is outlined in Paper[5]. In this model, the full cycle N is defined as the number of discharging and charging cycles required for the battery capacity to decrease from 100% to 80%. Thus, the wear battery model can be expressed as follows:

$$\dot{soh}(t) = -\frac{\mid P_i(t) \mid}{2E_0N(\mid P_i(t)) \mid)} \tag{4.16}$$

In Equation 4.16, $\dot{soh}(t)$ represents the derivative of the State of Health (SoH) function, $\mid P_i(t) \mid$ is the absolute value of the power for the battery module, and E_0 denotes the nominal capacity energy of the battery. The function $N(\mid P_i(t)) \mid)$

describes the relationship between the full cycle and the charging rate. Articles on battery lifetime analysis, such as [7], provide algorithms for this function. Given the same level of capacity degradation, a higher c-rate results in fewer cycles. However, this also varies with different battery models, each with its own parameters. Using the model provided in [7], a rough approximation of the full cycle function can be obtained. By collecting data on different full cycles, this function can be fitted as follows:

$$f(n) = 1828 * exp^{-0.0655n} \tag{4.17}$$

Equation 4.17 can be used to calculate the SoH. Consequently, Equation 4.16 can be expressed as follows:

$$\dot{s}oh(t) = -\frac{\mid P_i(t) \mid}{2 * E_0 * 1828 * exp^{-0.0655n}} \tag{4.18}$$

Equation 4.18 illustrates the modeling method of the battery SoH estimation. It aims to monitor real-time changes for the further balancing strategy.

4.2.2 Control Strategy for Current Allocation

Section 4.2.1 explains the principle for distinguishing the State of Health (SoH) during simulation. The next step is to address how to control battery modules with varying SoH. The control strategy is designed so that the fresh module provides more energy during charging, meaning its SoH decreases more rapidly than that of the aging module. In this thesis, where the power, voltage, and current of the battery modules remain constant, a straightforward method to resolve the imbalance is to supply power proportionally based on the SoH percentage of each battery cell. The main equation for this method is given in Equation 4.19.

$$SoH_n = \frac{SoH_n}{SoH_1 + SoH_2 + ... + SoH_n} \tag{4.19}$$

Figure 5.8 clearly shows that the SoH decreases over time. The rate of change is influenced by the load current, which is increased from 5A to 10A at 1 second, resulting in a corresponding boost in battery current. Consequently, the rate of SoH degradation increases. At 2 seconds, when the load current returns to its original value, the rate of SoH change matches that of the initial phase. The behavior is similar for the aging module, with the only difference being the initial SoH, which starts at 70%. Since in the thesis model, there are only two modules in the simulation. So the distribution equations are listed below:

$$SoH_1 = \frac{SoH_1}{SoH_1 + SoH_2} \tag{4.20}$$

$$SoH_2 = \frac{SoH_2}{SoH_1 + SoH_2} \tag{4.21}$$

5

Simulations

This chapter begins by presenting the identification results of the batteries. Next, it discusses the performance of the DC/DC converter, including the implementation of the PI controller and the load disturbance observer. Finally, the chapter introduces the results of the SoH balancing strategy.

5.1 Simulation Setup and Main Specifications

To determine whether the batteries are suitable for use in charging stations, a simulation in MATLAB must be conducted. In the simulations, 12 battery cells are connected in series to form a single battery module. One of these modules represents a fresh battery with 100% SoH, while the other represents an aged module with 98.65% SoH. These two modules are then connected in parallel within the load circuit. The parameters for the entire system are provided in Table 5.1.

Table 5.1: Main specifications

Parameters	Values
Number of battery cells in module	12
Power of the system	$50kW$
Output voltage of converter	$800V$
Input voltage of converter	$690V$
Input current of converter	$72A$
Inductance of converter	$4mH$
Capacitance of converter	$1mF$
Initial SoH in fresh module	100%
Initial SoH in aging module	98.65%
Conducted cycles of fresh module	0
Conducted cycles of aging module	1000

5.2 Verification of Battery Modelling

As described earlier, Kirchhoff's Current Law and the Ampere-hour equation can help to know the inductance and the capacitance.

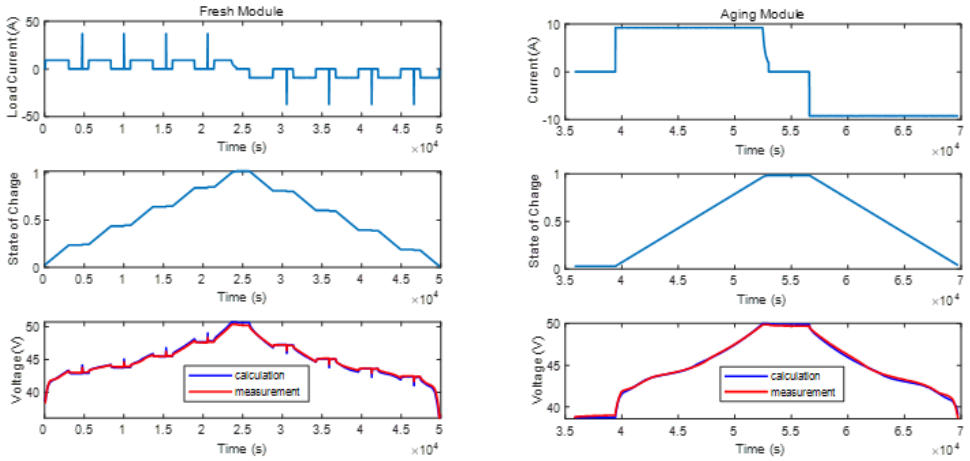

Figure 5.1: Results of the battery parameter identification.

Figure 5.1 illustrates the identification results for the battery module. As shown, the battery module begins charging when the SoC is at 0%, with both the voltage and SoC gradually increasing. Over time, the battery becomes fully charged as the SoC reaches 100%. Afterward, the battery begins to discharge, causing the voltage and SoC to gradually decrease. By comparing the SoC and voltage figures, it is evident that the changes are correlated. This confirms that the parameter results are accurate. The final results are presented in Table 5.2.

Table 5.2: Battery Parameters

Components	Values(Fresh)	Values(Aging)
R_0	0.02Ω	0.021Ω
R_1	0.02Ω	0.02Ω
R_2	0.01Ω	0.51Ω
C_1	$25000F$	$25000F$
C_2	$25000F$	$1000F$
$Capacity$	$37Ah$	$36.5Ah$

Compared the values respectively from the fresh module and aging module, battery aging causes capacity reduction, losing 0.5Ah after 1000 cycles. Meanwhile, Since the dynamic response time of the battery does not change, the capacitance decrease by 82% when the internal resistance increases from 0.01Ω to 0.51Ω due to aging.

5.3 Verification of Voltage and Current Control Loops in Buck-Boost Converters

This section presents the simulation results for the DC/DC converter, focusing on the functionality of the PI controller and the load disturbance observer.

In the current controller, the input signal is the inductor current, while the output signal is the modulation signal, which controls the conduction time of the power electronics. The primary function of the current controller is to adjust the inductor current to match the reference value. The results of this process are illustrated in Figure 5.2.

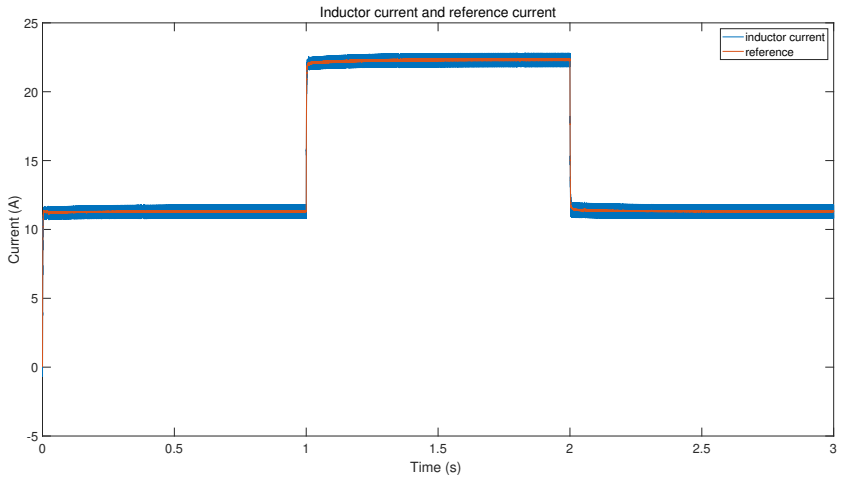

Figure 5.2: Results for the current controller.

It can be observed that the red line represents the reference current, while the blue line indicates the inductor current. To evaluate the performance of the current controller, the load current is increased from 5A to 10A at 1 second, and then decreased from 10A to 5A at 2 seconds. Regardless of whether the load current is increasing or decreasing, the inductor current closely follows the reference current, demonstrating the effectiveness of the current controller.

Having validated the performance of the current controller, the next step is to assess the voltage controller. The results of the DC/DC converter are shown in Figure 5.3.

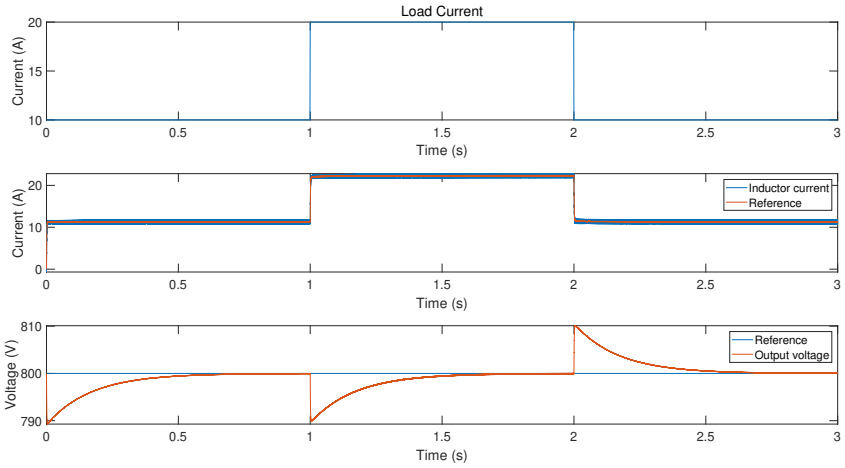

Figure 5.3: Results for the voltage controller.

In the voltage figure, the red line represents the output voltage, while the blue line indicates the reference voltage. The output voltage remains stable around 800V. Since the system's power remains constant, with the load increasing at 1 second and decreasing at 2 seconds, the output voltage is expected to decrease at 1 second and increase at 2 seconds. This behavior is clearly depicted in the figure, confirming that the voltage PI controller is functioning effectively. In conclusion, the entire DC/DC converter operates as expected.

5.4 Performance of Anti-Load Disturbance Compensation

Figure 5.3 shows that the rise time of the output voltage is approximately 0.5 seconds, which is relatively long for a 3-second simulation. Therefore, it is necessary to add a compensation loop to shorten the rise time. The effects of the observers are illustrated in Figure 5.4 and Figure 5.5, respectively.

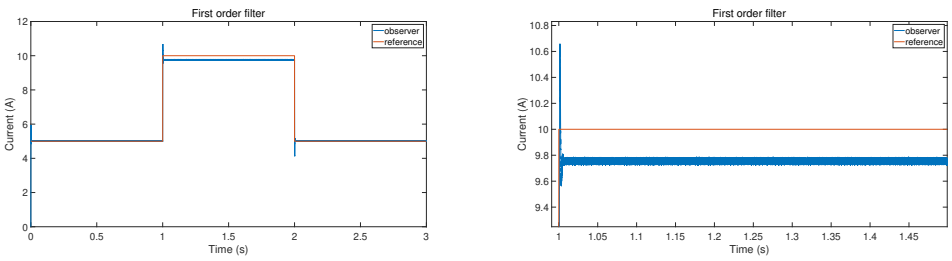

Figure 5.4: Observer with the first order filter.

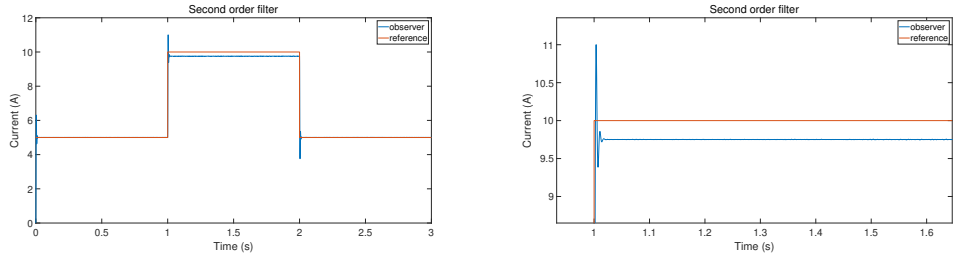

Figure 5.5: Observer with the second order filter.

When comparing the first-order and second-order systems, each has its advantages and disadvantages. The first-order system is easier to design, but its observation results are less ideal. In contrast, the second-order system is more complex to design, but it yields significantly better results in the observer. Therefore, the second-order system is chosen for the simulation.

As discussed, the second-order filter is implemented in the compensation part, and the resulting output is shown in Figure 5.11.

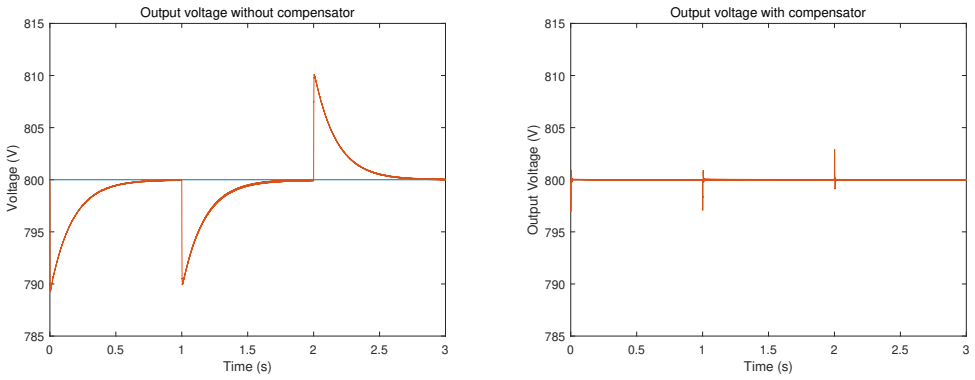

Figure 5.6: Output voltage without & with compensator.

Figure 5.6 clearly shows that the ripple voltage has decreased to approximately 4V, compared to the original ripple of about 10V. Additionally, the output voltage now reaches 800V almost instantly, whereas the original system took around 0.2 seconds to achieve this, which is significant in a 3-second simulation. This demonstrates that the disturbance compensation functions effectively in this model.

Finally, stability is crucial for the entire system. Once the transfer function is determined, the Bode diagram can be easily plotted to assess stability, as shown in Figure 5.7.

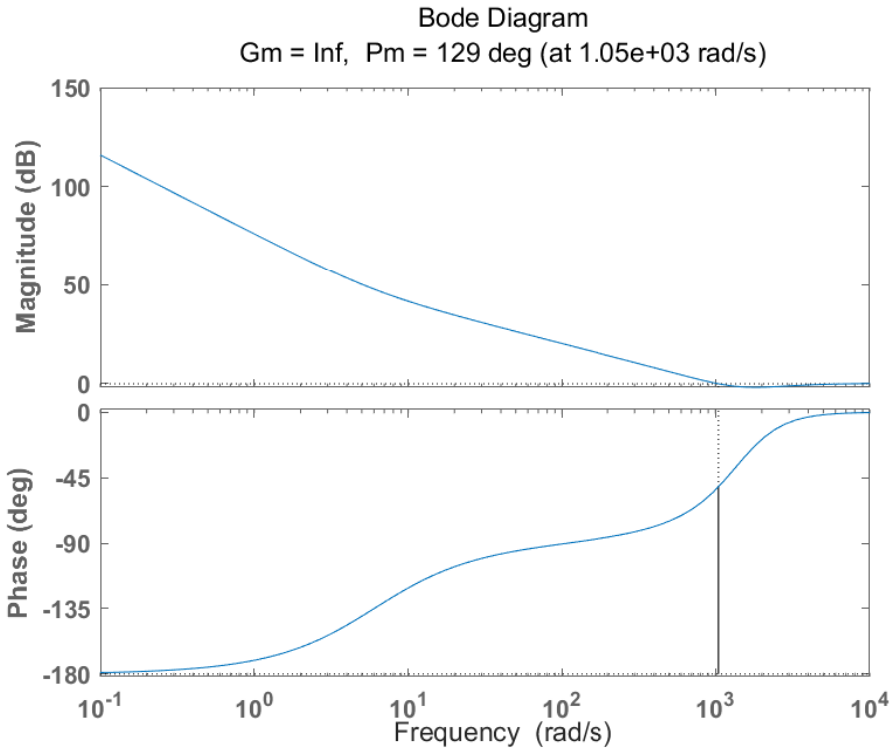

Figure 5.7: Bode diagram with the compensation loop.

Compared to the Bode diagram of the voltage controller, the frequency has shifted slightly, but it remains approximately ten times that of the current controller. This indicates that the system remains stable.

5.5 Verification of Current Allocation between Battery Packs

Before analyzing the results of the control strategy, it is important to first review the estimation results. The results for the fresh battery module are shown in Figure 5.8. Figure 5.10 illustrates the varying degradation speeds after applying the current distribution strategy, assuming a consistent aging rate at different stages. This indicates that the control loop is functioning correctly. However, the simulation duration of approximately 3 seconds is somewhat brief. At the end of simulation, the Soh of Fresh module is about 99.999% reducing by 0.01% while the aging Soh is 98.639%, reducing by 0.0096%. If the simulation could extend for hours, the State of Health (SoH) of the different battery modules would likely equalize, leading to a more balanced power supply distribution. Additionally, the output voltage must be evaluated before drawing final conclusions. The output voltage with the SoH balancing strategy is presented in Figure 5.11.

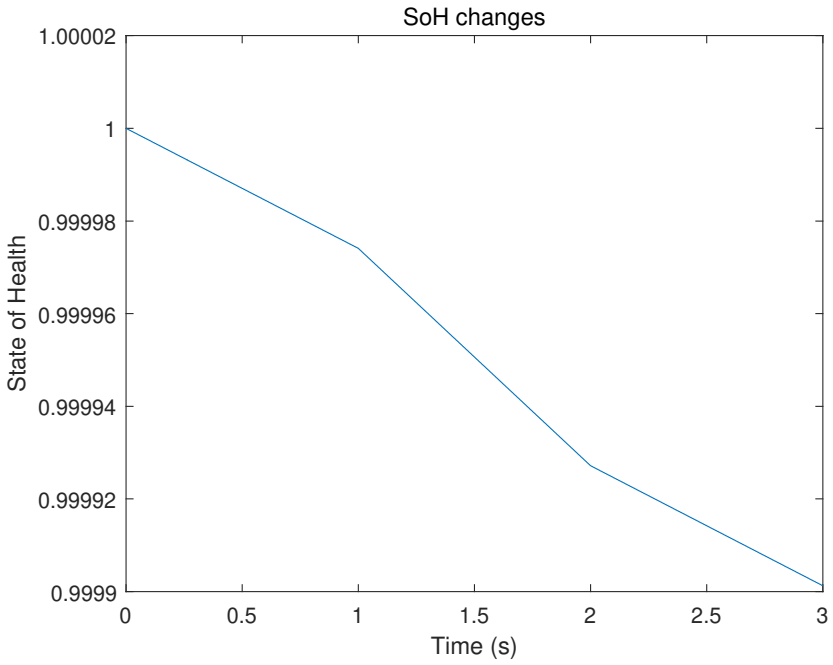

Figure 5.8: Result of SoH estimation.

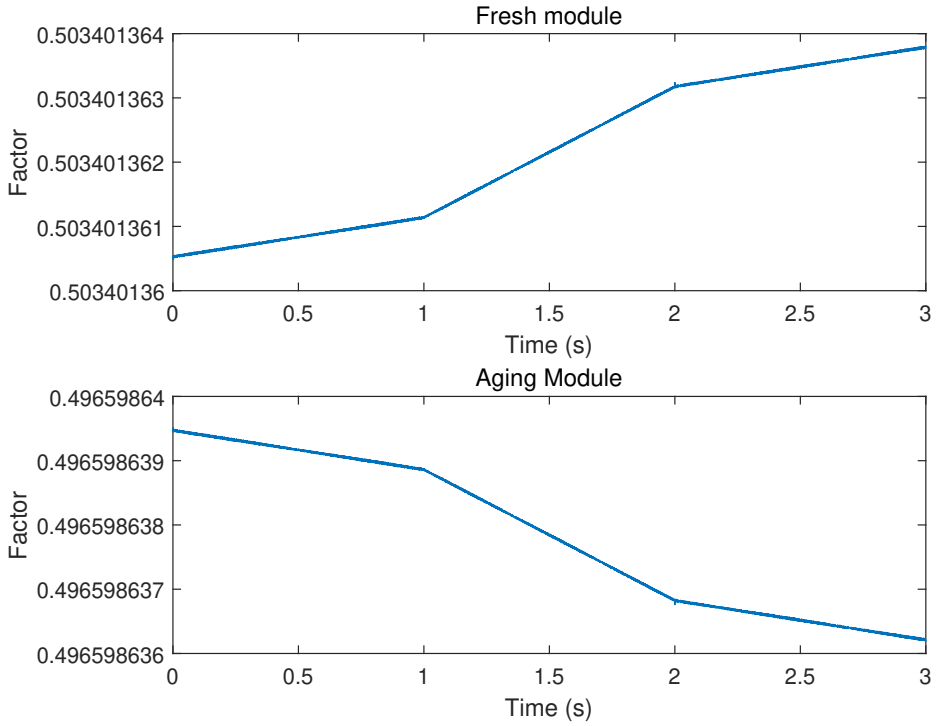

Figure 5.9: Result of SoH balancing factor.

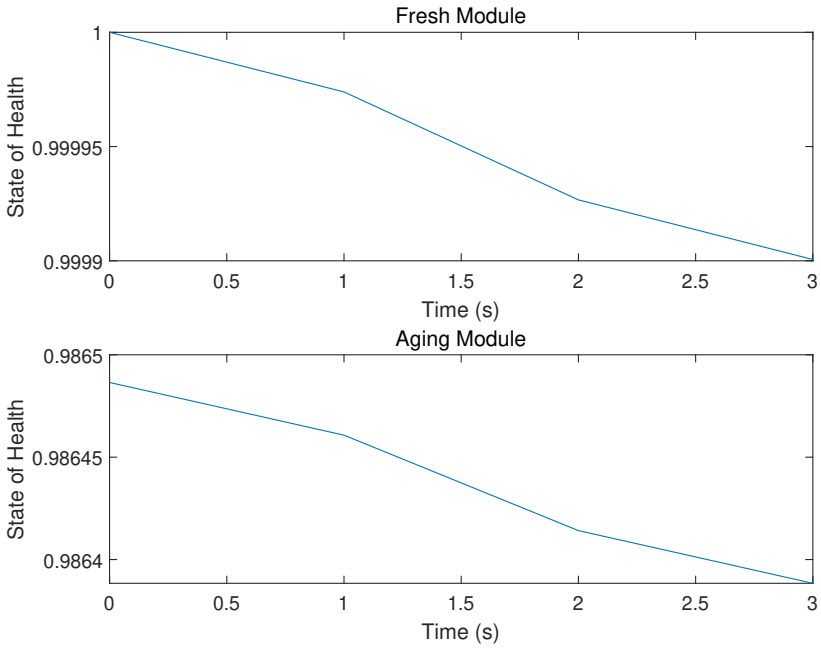

Figure 5.10: Comparison between fresh module and aging module.

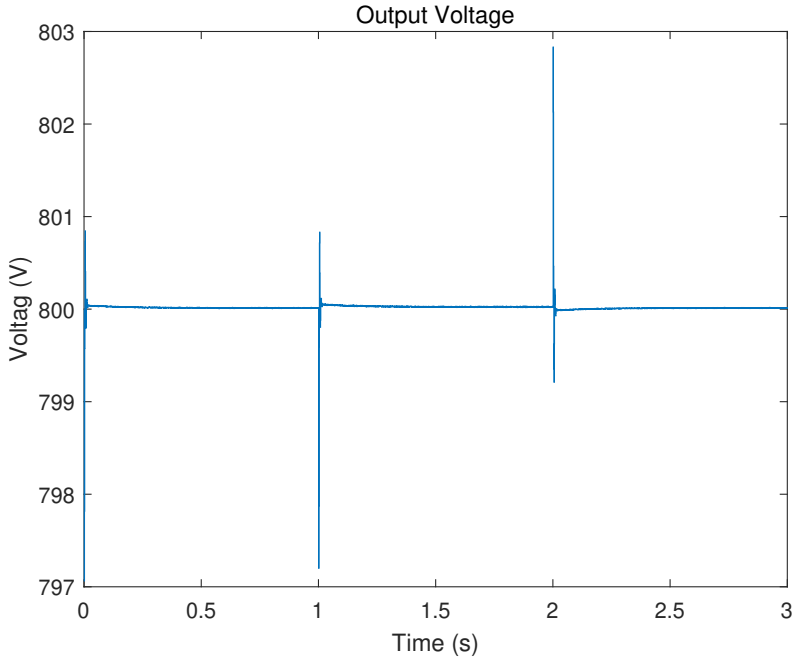

Figure 5.11: Compensated output voltage.

It is evident that the voltage remains stable around 800V, even with the addition of

the new control components. In conclusion, all components of the simulation work harmoniously together, yielding optimal results.

6

Conclusion and Future work

This chapter summarizes the work presented in this thesis and some suggestions for future work.

6.1 Conclusion

There are mainly three aspects presented in this thesis: Battery modeling, DC/DC converter design and integration battery modules in the charging station. The main conclusions are summarized below.

The results of the battery modeling show that:

- In terms of battery reusing, the second life battery solve the problem of wasting battery material and saving resources to become environmentally friendly. It's exploited to its full life time and significantly reducing the cost for installing and manufacturing.
- The second order of the battery model is built in this thesis, which leads to the identification of the internal resistance and capacitance. The degradation process will exhibit specific changes in internal impedance. Since the dynamic response time of the battery does not change, the capacitance decrease by 82% when the internal resistance increases from 0.01 Ω to 0.51 Ω due to aging, influencing the behaviour of the batteries, but causing very tiny changes in the DC/DC converter, especially for the high voltage applications.

The results of the DC/DC converter can tell that:

- During the designing for the converter parameters, power and voltage needs serve the important role in this process. What's more, the selection also requires to take the manufacturing values into consideration.
- The PI controller plays a vital role in the power electronics simulation. For the current controller which should be set first to see if the inductor current can reach the reference current calculating from the power and voltage. After adjusting the current controller, the voltage controllers also matters for the whole simulation. The overshoot is about 10V when the load decreases and undershoot is also 10V when the load increases.
- Stability is also one of the most important criterion to judge if the converter can continuously perform well. Bode Diagram shows the robustness of the whole system by presenting if the crossing frequency is close to the original one.

- The rise time can be significantly improved by incorporating the load disturbance observer. After implementing the compensation component, the regulation time is reduced from 0.5 seconds to approximately 0.01 seconds. Additionally, when the load decreases, the overshoot initially reaches around 10V. With the addition of the compensator, this overshoot is reduced to 3V. The same improvement is observed for the undershoot.

The results of the integration parts show that:

- Load disturbance observer function well to compensate the voltage and the voltage overshoot/undershoot has reduced by 70%.
- The SoH balancing presented in this work roughly solve the problem of integration for different battery modules. The batteries with better health state should supply more. As long as the battery modules have the same health state, they can shoulder the power supply equally.

6.2 Future Work

Based on the work finished in this thesis, the following steps can be considered and conducted in the future:

- The battery identification process can be enhanced, as the accuracy of the model in this thesis is not optimal. Improving the model's accuracy would make the comparisons between fresh and aging parameters more distinct and meaningful.
- Further efforts can be directed toward improving SoH balancing. The strategy proposed in this thesis is relatively simple. Depending on specific requirements, additional control mechanisms can be integrated to enhance the balancing process.
- The simulation currently lasts only about 3 seconds. To fully observe the entire charging and discharging process, a longer simulation duration should be considered.-+*++++-49-

Bibliography

[1] Federico Baronti, Roberto Di Rienzo, Nicola Papazafiropulos, Roberto Roncella, and Roberto Saletti. Investigation of series-parallel connections of multi-module batteries for electrified vehicles. In *2014 IEEE International Electric Vehicle Conference (IEVC)*, pages 1–7. IEEE, 2014.

[2] Sanjaya Bhattarai and Ngalula Sandrine Mubenga. Review of equalization techniques applied to second-life ev battery packs and their efficiency. In *NAECON 2023 - IEEE National Aerospace and Electronics Conference*, pages 10–15, 2023.

[3] NREL Transforming Energy. Transportation and mobility research, 2021. `https://www.nrel.gov/transportation/medium-heavy-duty-vehicle-charging.html` [Accessed: (2024.7.16)].

[4] Roland Irle. Global evs sale for 2023, 2024. `https://ev-volumes.com/news/ev/global-ev-sales-for-2023/` [Accessed: (2024.1.22)].

[5] Lars Johannesson, Nikolce Murgovski, Soren Ebbesen, Bo Egardt, Esteban Gelso, and Jonas Hellgren. Including a battery state of health model in the hev component sizing and optimal control problem. *IFAC Proceedings Volumes*, 46(21):398–403, 2013.

[6] Ravi Kumar Kanaparthi, Jay Prakash Singh, and Makarand Sudhakar Ballal. A review on multi-port bidirectional isolated and non-isolated dc-dc converters for renewable applications. In *2022 IEEE International Conference on Power Electronics, Drives and Energy Systems (PEDES)*, pages 1–6, 2022.

[7] Peter Keil, Simon F Schuster, CV Lüders, Holger Hesse, A Arunachala, and Andreas Jossen. Lifetime analyses of lithium-ion ev batteries. In *3rd Electromobility Challenging Issues conference (ECI)*, pages 1–5, 2015.

[8] Neil King. Evs forecast to accout for two thrirds of global light vehicle sales in 2035, 2023. `https://ev-volumes.com/news/ev/evs-forecast-to-account-for-two-thirds-of-global-light-vehicle-sales-in-2035/` [Accessed: (2024.11.21)].

[9] Dinesh Kumar, Firuz Zare, and Arindam Ghosh. Dc microgrid technology: system architectures, ac grid interfaces, grounding schemes, power quality, communication networks, applications, and standardizations aspects. *Ieee Access*, 5:12230–12256, 2017.

[10] Idoia San Martín, Elisa Braco, Álvaro Martin, Pablo Sanchis, and Alfredo Ursúa. Integration of second-life batteries in residential microgrids and fast charging stations. In *2022 IEEE International Conference on Environment and Electrical Engineering and 2022 IEEE Industrial and Commercial Power Systems Europe (EEEIC / CPS Europe)*, pages 1–6, 2022.

[11] Mohamed AA Mohamed, Tung Fai Yu, and Thomas Grandjean. Pso-tuned variable forgetting factor recursive least square estimation of 2rc equivalent circuit model parameters for lithium-ion batteries. In *2023 IEEE Vehicle Power and Propulsion Conference (VPPC)*, pages 1–6. IEEE, 2023.

[12] Shannon Osaka. After a century of growth, have carbon emissions reached their peak?, 2020. `https://grist.org/climate/was-2020-the-year-we-reached-peak-carbon-emissions/` [Accessed: (2020.12.29)].

[13] Jens F Peters, Manuel Baumann, Benedikt Zimmermann, Jessica Braun, and Marcel Weil. The environmental impact of li-ion batteries and the role of key parameters–a review. *Renewable and Sustainable Energy Reviews*, 67:491–506, 2017.

[14] Ounis Rabiaa, Ben Hamed Mouna, Sbita Lassaad, Flah Aymen, and Abid Aicha. Cascade control loop of dc-dc boost converter using pi controller. In *2018 International Symposium on Advanced Electrical and Communication Technologies (ISAECT)*, pages 1–5, 2018.

[15] Marek Rybárik, Peter Braciník, and Martina Kajanová. Overview of the usability of second-life batteries in smart distribution grids. In *2022 ELEKTRO (ELEKTRO)*, pages 1–4, 2022.

[16] Thomas A Stuart and Wei Zhu. Fast equalization for large lithium ion batteries. *IEEE Aerospace and Electronic Systems Magazine*, 24(7):27–31, 2009.

[17] Xiangdong Sun, Yonghang Zhou, Guitao Chen, and Biying Ren. Model predictive control of a phase-shifted full-bridge dc-dc converter. In *2020 IEEE 9th International Power Electronics and Motion Control Conference (IPEMC2020-ECCE Asia)*, pages 2710–2714, 2020.

[18] K Suresh and R Arulmozhiyal. Design and implementation of bi-directional dc-dc converter for wind energy system. *Circuits and Systems*, 7(11):3705–3722, 2016.

[19] wallbox. Ev charging current: What's the difference between ac and dc?, 2024. `https://wallbox.com/en_sg/faqs-difference-ac-dc` [Accessed: (2020.12.29)].

[20] Siyu Wu, Kangan Wang, Yixian Qu, Rongwu Zhu, Wei Tan, Weimin Wu, and Marco Liserre. Topology and operation analysis of isolated dc/dc converters with bidirectional asymmetric power flow. In *IECON 2022–48th Annual Conference of the IEEE Industrial Electronics Society*, pages 1–5. IEEE, 2022.

[21] Yefan Wu, Zhigang Liu, Jian Chen, Shuyun He, Yifan Wang, and Hui Hou. Overview of charging and discharging dispatching strategies for electric vehicles. In *2021 IEEE 4th International Electrical and Energy Conference (CIEEC)*, pages 1–5, 2021.

[22] S Xu, H Zhang, D Shi, X Guo, X Lin, Z Li, et al. Setting strategy of charging service fee for fast charging load of smart cities. *Proceedings of the CSEE*, 40(10):3187–3201, 2020.

[23] Qian Xun, Yujing Liu, and Xiaoliang Huang. Intelligent power allocation with load disturbance compensator in fuel cell/supercapacitor system for vehicle applications. In *2020 IEEE Transportation Electrification Conference & Expo (ITEC)*, pages 489–494. IEEE, 2020.

[24] HAJI Zakaria, MOUNIR Hamid, EL MARJANI Abdellatif, and AMARIR Imane. Recent advancements and developments for electric vehicle technology. In *2019 International Conference of Computer Science and Renewable Energies (ICCSRE)*, pages 1–6, 2019.

[25] Xiaowei Zhao, Yishan Cai, Lin Yang, Zhongwei Deng, and Jiaxi Qiang. State of charge estimation based on a new dual-polarization-resistance model for electric vehicles. *Energy*, 135:40–52, 2017.

DEPARTMENT OF SOME SUBJECT OR TECHNOLOGY
CHALMERS UNIVERSITY OF TECHNOLOGY
Gothenburg, Sweden
www.chalmers.se

CHALMERS
UNIVERSITY OF TECHNOLOGY